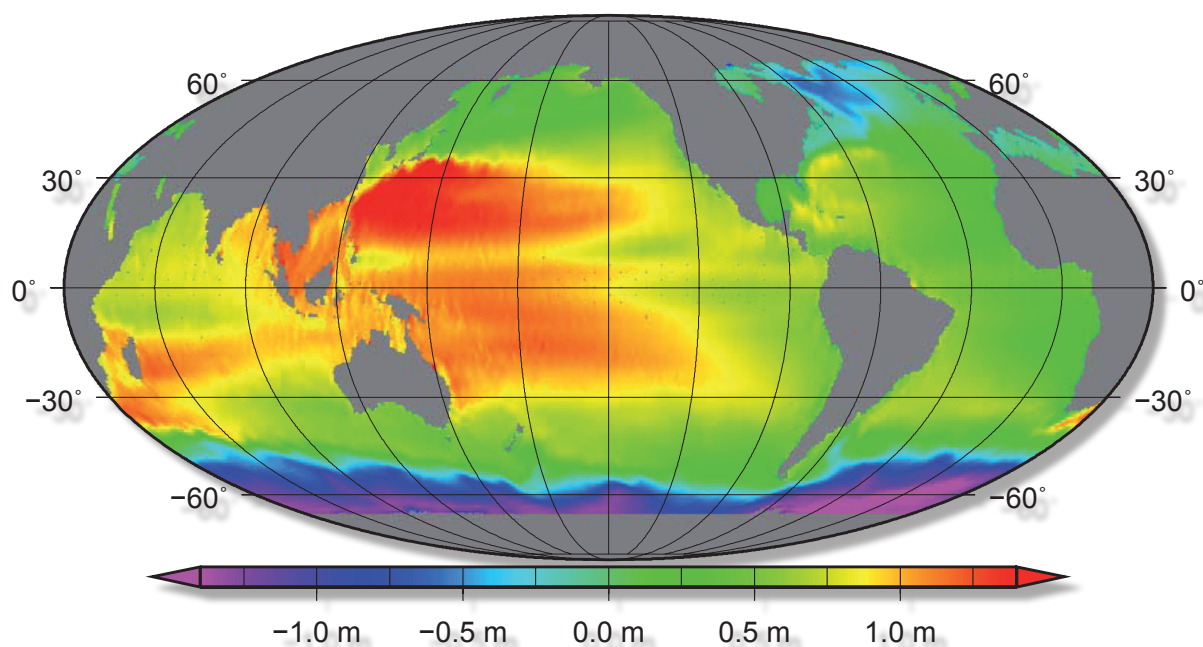# DGFI Report No. 82 / IAPG FESG Report No. 27

Dynamic Ocean Topography - The Geodetic Approach

ALBERTA ALBERTELLA[1], ROMAN SAVCENKO[2],
WOLFGANG BOSCH[2], REINER RUMMEL[1]

[1]Institut für Astronomische und Physikalische Geodäsie (IAPG)
[2]Deutsches Geodätisches Forschungsinstitut (DGFI)
München 2008

Table of Contents

2nd Edition

1 Introduction

The determination of global dynamic ocean topography (DOT) is of fundamental importance for ocean and climate research. The idea to derive it from the combination of satellite altimetry and precise geoid models is already discussed in the famous Williamstown Report [Kaula, 1970]. Since then this idea has been a strong argument for the development of more and more sophisticated satellite altimetry and more and more refined geoid models.

The concept has been analyzed in depth in a fundamental paper by [Wunsch and Gaposchkin, 1980]. The realisation of this concept was one of the basic motivations which led to the development and realization of the current gravity field satellite missions CHAMP, GRACE and GOCE.

For the preparation of the GRACE and GOCE missions, a number of oceanographic simulation studies have been carried out [Ganachaud et al., 1997, Le Grand and Minster, 1999, Le Provost et al., 1999, Le Grand, 2001, Schröter et al., 2002]. They investigated the complete processing chain from the combination of geoid and altimetric sea surface height via the assimilation into circulation models to the determination of oceanic transports, based on various assumptions for the geoid accuracy and spatial resolution. The studies demonstrated that the new satellite geoid models will allow the determination of geostrophic surface velocities with an accuracy of a few cm/s. GOCE with its expected high spatial resolution should allow the recovery of details down the spatial scales of about 100 km.

In order to be of relevance for ocean modelling the combination of altimetry and geoid model must be achieved with highest possible precision and spatial resolution. In principle the basic relationship is very simple, it is

$$\zeta = h - N \tag{1}$$

where ζ is assumed to be the steady-state DOT, h is the altimetric height above an adopted reference ellipsoid and corrected for all short time variable effects such as tides and N are the geoid heights referred to the same reference ellipsoid. However, thereby the problem rises that the geoid model is usually provided as a truncated spherical harmonic series, i.e. in a band-limited global spectral representation on a sphere, while altimetric measurements are given as point values, or more accurately as weighted mean values over the footprint of the radar signal, along the ground track of the spacecraft. Their sample rate is very high along the track and rather coarse in cross track direction.

For the determination of DOT the two representations have to be made spectrally consistent, i.e. both the geoid model and altimetry signals have to cover the same spectral range. Since altimetry measurements contain information with higher spatial resolution than is included in the geoid model, these short scale features are to be removed by filtering.

In constructing a geoid model, one truncates its spectrum at a certain maximum degree L. For all degrees less or equal to L one has the coefficients of the model together with their error (commission error). The signal for degrees greater than L is not modelled, but its expected average size is identified as omitted signal (omission error). Different models exist for the omission error and it can be large depending on the cut-off degree L. The scales that are suppressed by filtering become "omission" and must be taken in account

in the total error budget. Previous research, [Losch et al., 2002], has shown that a portion of the omission error can leak into the commission error of the filtered signal, if several systems of base functions are involved. Why is this consistency so important? Geoid heights truncated at L are missing the signal part above L; it has been omitted. Subtracting such geoid heights from the altimetric sea surface heights means that a part missing in the geoid signal is not removed from the altimetric heights. It causes a non-random error that would be mis-interpreted as a part of the DOT.

Furthermore the DOT determined in this way needs to be spectrally consistent with the ocean circulation model (OCM) into which the dynamic ocean topography is to be assimilated. While the former aspect is discussed, e.g. in [Ganachaud et al., 1997, Losch and Schröter, 2004, Wunsch and Gaposchkin, 1980, Wunsch and Stammer, 1998], the latter question has not been addressed so far in the literature.

What does spectral consistency mean? It depends, because the combination of geoid model and altimetry can be done employing various spectral representations, such as along profiles (1D-Fourier model), in boxes (2D-Fourier model), on the sphere and globally (SH-analysis), using principal component analysis over ocean basins, wavelets, a.s.o. The outcome may therefore depend on the chosen representation.

Now one may argue, why not simply apply the same filters to the geoid model and to altimetry (either 1D, 2D or on a sphere). This may look like a reasonable idea at first sight, but one should realize that each filter has to meet certain mathematical conditions, e.g. to be periodic for 1D-FFT, and if these conditions are not met certain distortions will enter the data.

An obvious difficulty in this respect is the fact that the geoid models are given globally while altimetry profiles are limited to the oceans. As coastal areas are of particular importance for the understanding of ocean dynamics, any processing of DOT should try to avoid mathematical distortions to enter there.

A concise definition of the posed problem is as follows: how to optimally combine a global data set which possesses a certain (low) spectral resolution with a regional (or not-global) data set with much higher spectral resolution?

2 Altimetry data pre-processing

During the past few decades, satellite altimetry has been developed to a powerful technique to precisely observe the ocean surface and to monitor the sea level variations. State-of-the-art altimeter systems allow deriving sea surface heights with a precision of a few centimetres.

However, every mission has inherent sampling problems: first the lifetime of satellites is usually designed for a period of 3 – 5 years such that data from a single mission is not sufficient to provide a representative long-term mean on the ocean surface (the 13 years lifetime of TOPEX is an exception). Second, due to orbit dynamics the ground track configuration must solve the trade-off between high spatial and high temporal resolution. For example, with a ten day repeat cycle TOPEX priority was on a high temporal resolution and de-aliasing of ocean tides – at the cost of an equatorial ground

track spacing of more than 300 km. Finally, the pulse limited radar altimeter systems are essentially observing profiles and leave large diamond shaped areas unobserved. All this strongly suggests a combination of consecutive altimeter missions or of missions with different, complementary sampling characteristics.

Such a combination requires three pre-processing steps: upgrading, harmonization and cross-calibration. DGFI has access to all data from ERS-1, ERS-2, TOPEX/Poseidon, ENVISAT, GFO, Jason-1, and other missions. All data is administrated in a mission independent format with parameter values split into individual files. This allows an easy replacement of single record parameters without the need to change the complete data base. This way, upgrading of new orbits (for the ESA missions), time tag corrections (for ERS-1/2) and improved correction models for the microwave radiometer (TOPEX) has been accomplished (compare Table 1). Harmonization implies to use as far as possible the same models for geophysical corrections to avoid that model differences are wrongly interpreted as apparent sea level variations. Therefore, for all missions the inverted barometer correction was replaced by the dynamic atmospheric corrections (DAC) produced by CLS Space Oceanography Division using the MOG2D model from LEGOS [Carrère and Lyard, 2003]. Moreover, the ocean tide corrections for all missions were based on the FES2004 [Lyard et al., 2006] – a de-facto standard in satellite altimetry and gravity field modelling. Table 2.1 summarizes all efforts to upgrade and harmonize the altimeter data. Finally, a cross calibration was performed by a global crossover analysis based on nearly simultaneous single- and dual satellite crossover differences performed between all altimeter systems operating contemporaneously. This crossover analysis captures not only relative range biases, but also systematic inconsistencies in the center-of-origin realization and geographically correlated errors. Through this cross calibration the radial errors of all satellites became available for the complete TOPEX lifetime. It is straightforward to estimate an empirical error covariance function using the complete history of radial errors. The error covariance function, derived from the time series of radial errors is valuable information for the error propagation discussed in section 6.2 below. Details of this multi-mission cross calibration are described in [Bosch and Savcenko, 2006].

Further enhancements of the altimeter data are possible. In deep ocean the ocean tides are assumed to be known to within 2 cm root-mean-square (RMS) uncertainty at wavelengths of 50 km [Shum et al. 2001]. However, over continental shelves and in polar oceans much larger deficiencies for ocean tides are well known – even for the most recent models like FES2004. Using the pre-processed altimeter data, DGFI performed a global empirical tide analysis and found significant residual ocean tide signals relative to FES2004 [Savcenko and Bosch, 2007, Bosch et al., 2008]. In shallow water

Table 2.1 Altimeter mission data and replacements for upgrading and harmonization

Mission (Phase)	Cycles	Period	Source	Replacements
TOPEX/Poseidon	001-481	1992/09/23-2005/10/08	MGDR-C AVISO	Chambers SSB correction, FES2004
Jason1	001-135	2002/01/15-2005/09/14	GDR-B PODACC	FES2004
ERS-1 (C & G)	083-101 144-155	1992/04/14-1993/12/20 1995/03/24-1996/04/28	OPR-V6 CERSAT	DEOS orbits, FES2004, pole tide, 1.5ms time bias
ERS-1 (D, E & F)	102-143	1993/12/25-1995/03/21	OPR-V3 CERSAT	DEOS orbits, FES2004, pole tide, 1.5ms time bias
ERS-2	000-085	1995/04/29-2003/07/02	OPR-V6 CERSAT	DEOS orbits, FES2004, pole tide, 1.3ms time bias
ENVISAT	009-040	2002/09/24-2005/09/19	GDR ESA/CNES	FES2004
GFO	037-159	2000/01/07-2005/10/04	GDR NOAA	FES2004

areas the M2 and S2 constituents show numerous extended patterns with residuals taking amplitudes of up to 15 cm. Other major constituents and the non-linear shallow water tide M4 hit residual amplitudes up to 5 cm. The results have been used to set up a new global ocean tide model, EOT08a [Savcenko and Bosch, 2008]. The new tide model will be applied as soon as the evaluation is completed.

Time series analysis of altimeter data is important, as it allows identifying and quantifying the sea level variability. High sea level variability complicates the reliable determination of the mean sea level and the estimation of a steady-state DOT. Moreover, the sea level variability must be known in order to design and apply filter which make the altimeter data consistent with the properties of the numerical model used to assimilate the sea level data. In order to facilitate the analysis of altimeter time series, the complete altimetry data base was re-organized. The sequential file structure (mission => 1:n => cycle) is not well suited as repeated measurements at neighbouring locations are distributed over all cycles. Therefore the data structure was reverted by defining small cells (so called BINs) along the nominal ground track and assembling all observations to those BINs whose centres are closest to the measurement locations (the locations of repeated observations do not exactly coincide). The along-track extension of these BINs is only some 7 km, such that the set of data within a BIN can be taken to estimate the mean, the variance, sea level trends or amplitudes and phases of seasonal periods or alias periods of tides.

From such time series analyses a few important information can be derived: Figure 2.1 shows the standard deviations for estimating a linear drift of sea level anomalies (SLA), the differences between instantaneous sea surface
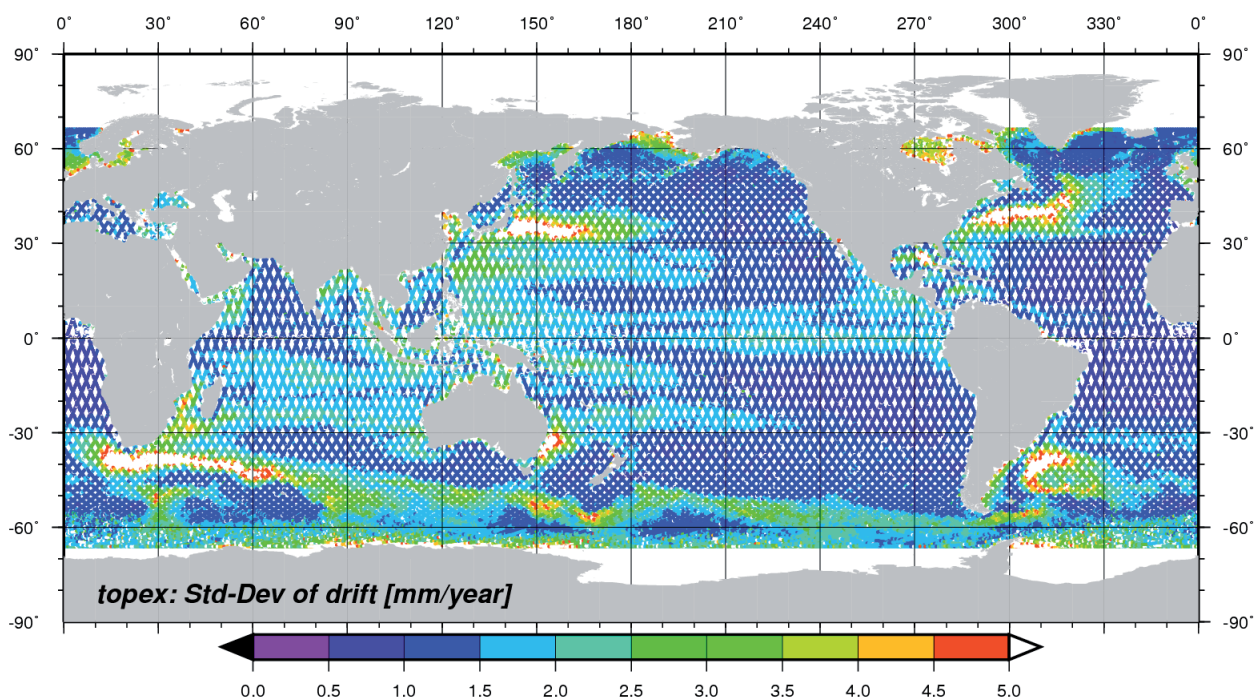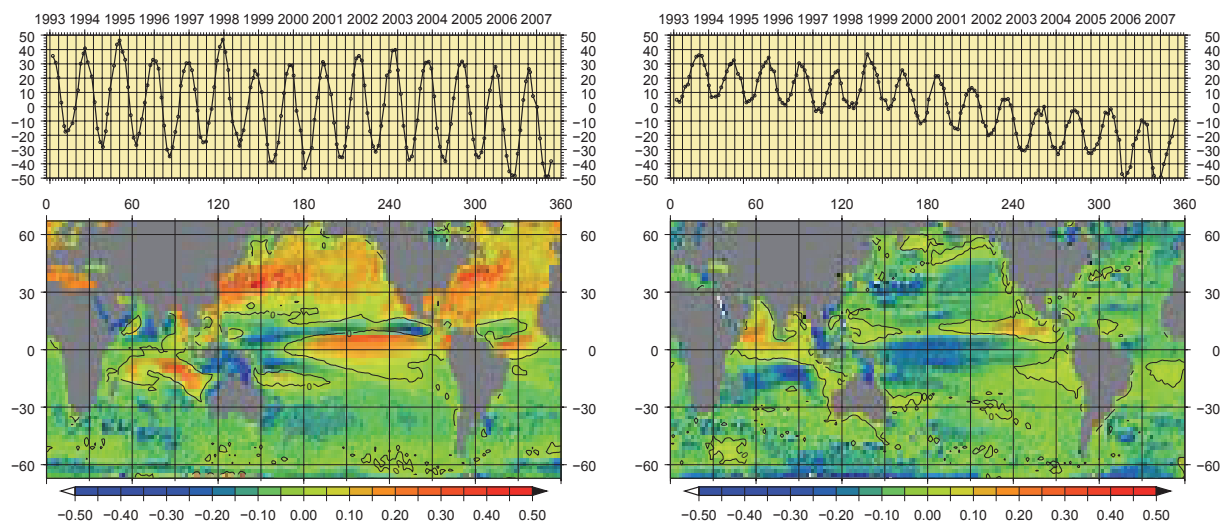

Fig. 2.1 The RMS values of sea level anomalies (differences between instantaneous sea surface heights and the CLS01 mean sea surface) can be taken as a measure of sea level variability.

Fig. 2.2 The first two, most dominant modes of a Principal Component Analysis of the TOPEX sea level anomalies capture together about 22% of the total variance of global sea level variations. The associated Principal Components (upper panels) exhibit for both modes a pronounced annual periodicity. The very first mode (left) explains the dominant annual sea level oscillation between northern and southern hemisphere.

heights and the CLS01 mean sea surface. These standard deviations are a good measure for the sea level variability. Fig 2.1 clearly shows the Western boundary currents and the Antarctic Circumpolar Current as areas of highest variability.

Figure 2.2 shows the seasonal variability. A time series of monthly mean values of the sea level anomalies were taken to perform a Principal Component Analysis(PCA). PCA identifies the most dominant pattern of sea level variability and shows by the principal components how these pattern change with time. Fig 2.2 shows the first two, most dominant modes. Together they capture about 22% of the total variability with a significant annual periodicity indicated by the associated Principal Components (top panels).

3 Geoid status

The Earth's gravitational potential is usually expressed [Heiskanen and Moritz, 1967] in terms of fully normalized spherical harmonic functions $Y_{lm}(\varphi,\lambda)$:

$$V(r,\varphi,\lambda) = \frac{GM}{R} \sum_{l=0}^{\infty} \left(\frac{R}{r}\right)^{l+1} \sum_{m=-l}^{l} y_{lm} Y_{lm}(\varphi,\lambda)$$

(3.1)

where l is the degree of the spherical harmonic, m is the order, and y_{lm} is the corresponding spherical harmonic coefficient. G is the gravitational constant, M the mass of the Earth and R the mean radius of the Earth; the latitude and the longitude of the considered point are φ and λ.

The spherical harmonic functions are defined as

$$Y_{lm} = \overline{P}_{l|m|}(\varphi) \begin{cases} \cos m\lambda & m \geq 0 \\ \sin|m|\lambda & m < 0 \end{cases}$$

(3.2)

with the fully normalized associated Legendre functions $\overline{P}_{l|m|}$.

The series coefficients allow the determination of geoid heights, above an adopted reference ellipsoid, with:

$$N(\varphi,\lambda) = R \sum_{l=0}^{\infty} \sum_{m=-l}^{l} y_{lm} Y_{lm}(\varphi,\lambda)$$

(3.3)

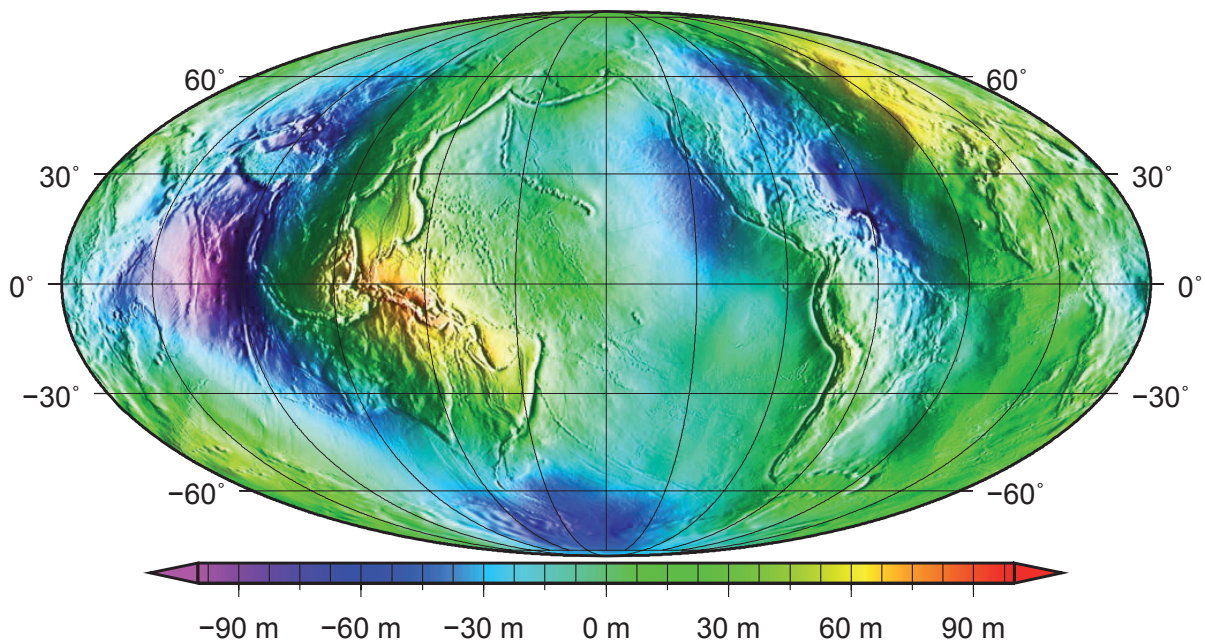The signal power density is expressed in terms of degree variances c_l, defined as

Fig. 3.1 Geoid undulations computed with the gravity field model EGM08.

$$c_l = \sum_{m=-l}^{l} y_{lm}^2$$

(3.4)

or in terms of their square roots, the root-mean-square (RMS) value per degree. It can be shown that on the Earth's surface the degree variances follow the rule of thumb, according to [Kaula, 1966]

$$c_l = 1.6 \frac{10^{-10}}{l^3} \quad .$$

(3.5)

When a geopotential model is given, the set of the coefficients y_{lm} up to a certain maximum degree L is available. The use of the coefficients to a maximum degree, L, causes an omission error (i.e. the effect of neglected higher degree coefficients) in the computed undulation, while the errors in the potential coefficients create a commission error in the computed geoid undulations.

Together with the finite set of harmonic coefficients there must be given their variance-covariance matrix with dimension equal to $(L+1)^2 \cdot (L+1)^2$. This covariance matrix is a full matrix, but with a block-diagonal predominance. It contains the error variance σ_{lm}^2 of each coefficient y_{lm} and all its error covariances cov$\{y_{lm}, y_{nk}\}$ with the others coefficients.

Disregarding the correlations, in a simplified scheme, for each degree l, we define the error degree variances as

$$\varepsilon_l = \sum_{m=-l}^{l} \sigma_{lm}^2$$

(3.6)

In Fig.3.1 are shown the geoid undulations computed with the recently publishes ultra-high resolution gravity field model EGM08, [Pavlis et al., 2008]. The model is available up to degree and order 2160 (corresponding to a spatial resolution of 5'x5') and was generated by combining a satellite only gravity field and surface gravity data.

In the following we consider these geopotential models:

1) **EGM96**. It is a model consisting of spherical harmonic coefficients complete to degree and order 360, computed by National Imagery and Mapping Agency, the NASA Goddard Space Flight Center and the Ohio State University. The model incorporates surface gravity data, satellite tracking data and satellite altimetric observations.

2) **EIGEN-GRACE02s**. It is a satellite only gravity model complete to degree and order 150 from GRACE, realised in 2005 by GFZ Potsdam, [Reigber et al., 2005].

3) **GOCE**. It is a geopotential model derived from a simulation study of the next satellite gravity mission GOCE. In this case the observable is the measurement of gravity gradient based on differential accelerometry. This concept allows high resolution determination of the gravity field with homogeneous accuracy. The expected degree resolution is about degree 200 to 250.

In Fig. 3.2 are shown the error degree variances of the EGM96, GRACE and (simulated) GOCE models compared with the signal power density of the Kaula rule (3.5). The points of intersection between the degree error curves

and the Kaula's line define the resolution of the geopotential model.

In order to see how the error ε_l accumulates over the degree l, we define the cumulative commission error in a certain bandwidth as:

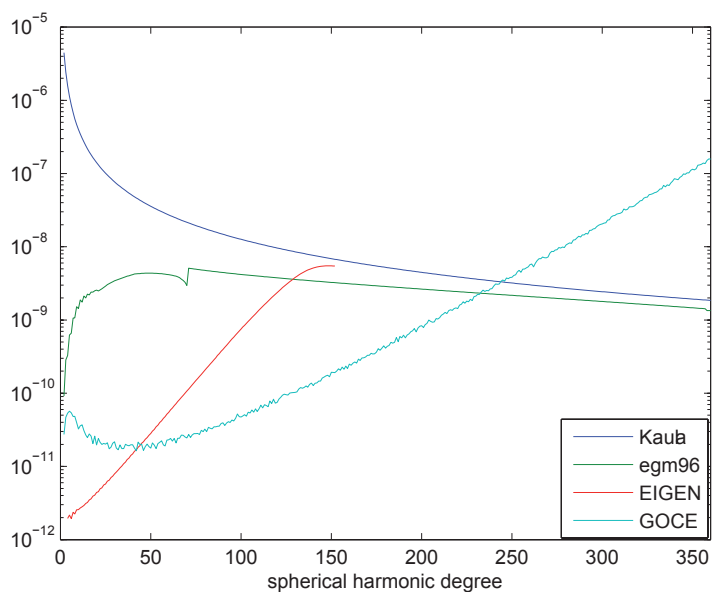$$CUM_L = \sqrt{\sum_{l=2}^{L} \varepsilon_l}$$

(3.7)

Figure 3.2 RMS of the degree errors for the geopotential models: EGM96, EIGEN and GOCE together with the signal RMS from eq. (3.5).
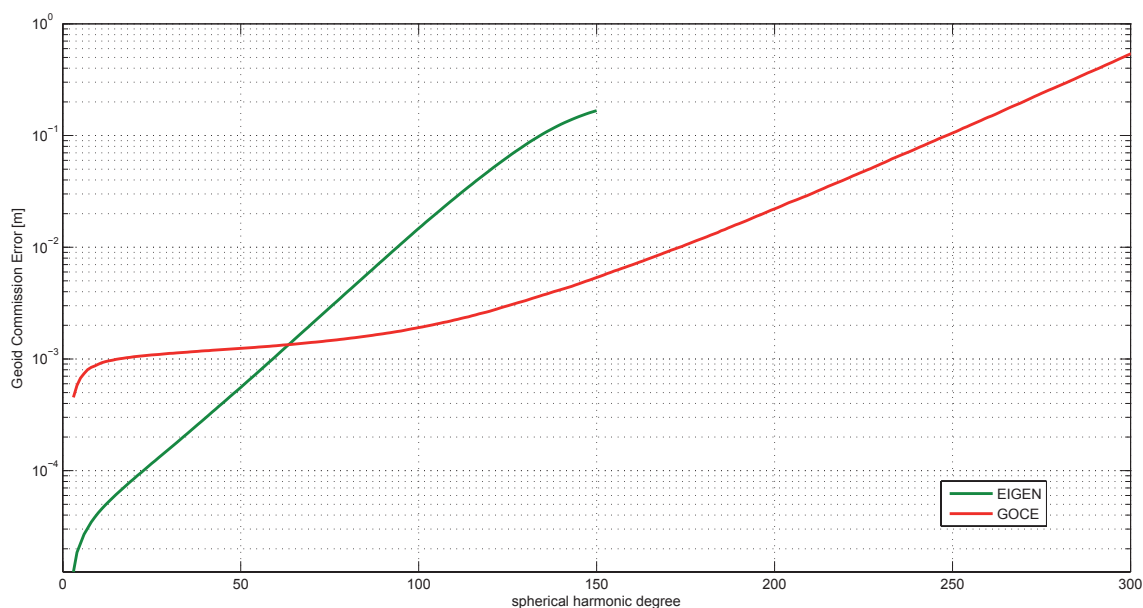

Figure 3.3: The cumulated commission error for geoid undulations computed from EIGEN and GOCE geopotential models.
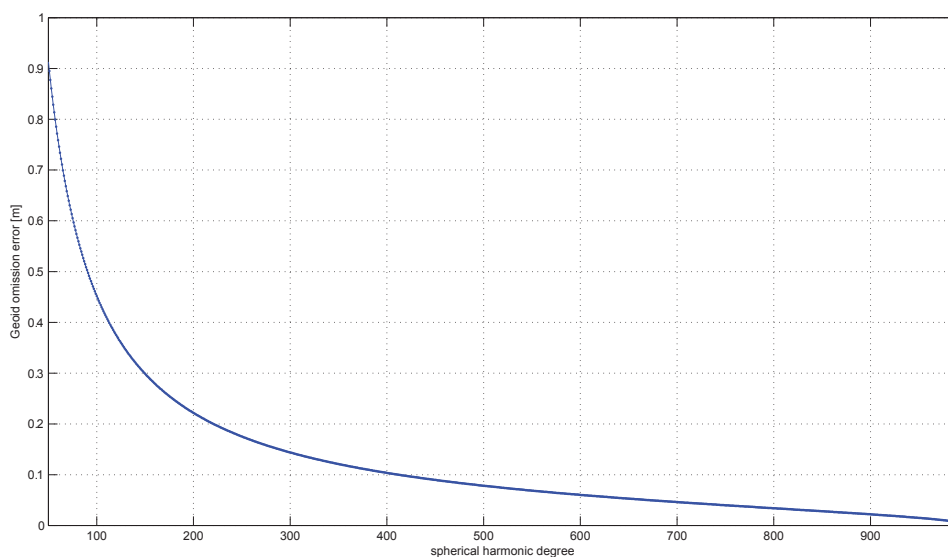
Figure 3.4: Omission error for the geoid undulations as function of the cut-off degree L, computed using Kaula's rule.

that, for the geoid undulation, becomes:

$$CUM_L^{(N)} = R\sqrt{\sum_{l=2}^{L} \varepsilon_l}$$

$$(3.8)$$

In Fig. 3.3 are shown the cumulative geoid commission errors for EIGEN and GOCE models.

However we have to consider the second part of the error due to the limitation in the harmonic expansion. The real field is composed by infinite terms, while the estimated model must to be finite and therefore it has a cut-off degree *L*.
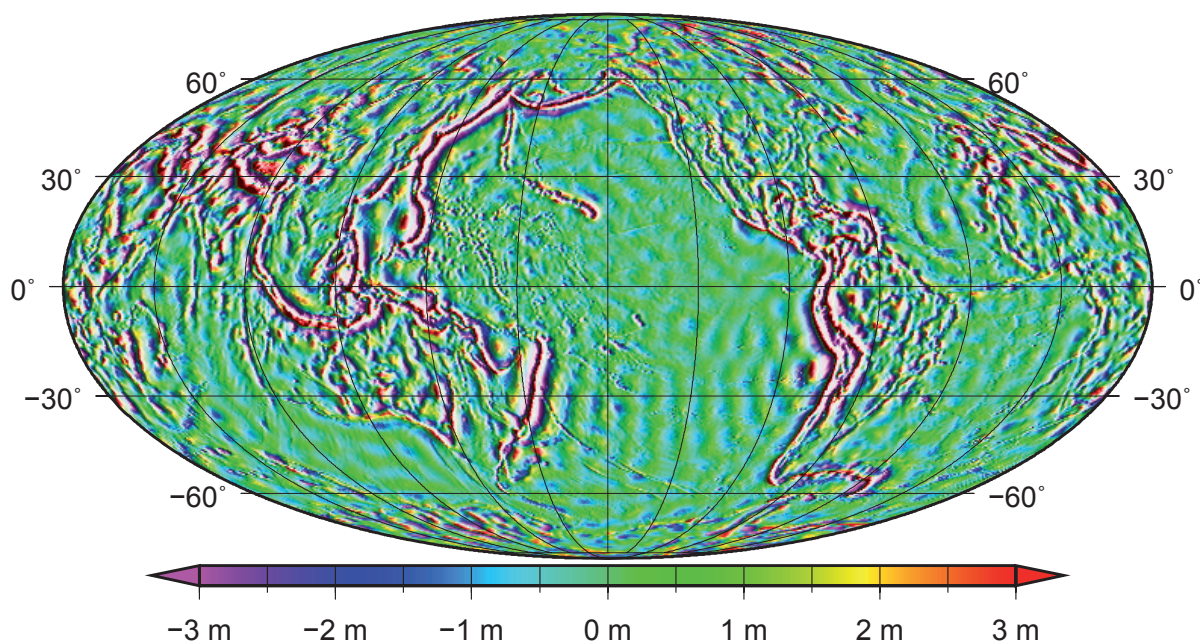

Fig. 3.5 Omission error for a cut-off at degree 45, estimated from the ultra high resolution gravity field model EGM08

We can write the eq. (3.3) as

$$N(\varphi,\lambda) = R\sum_{l=0}^{L}\sum_{m=-l}^{l} y_{lm}Y_{lm}(\varphi,\lambda) + R\sum_{l=L+1}^{\infty}\sum_{m=-l}^{l} y_{lm}Y_{lm}(\varphi,\lambda)$$

We define as omission error the expected signal power that has not been modelled:
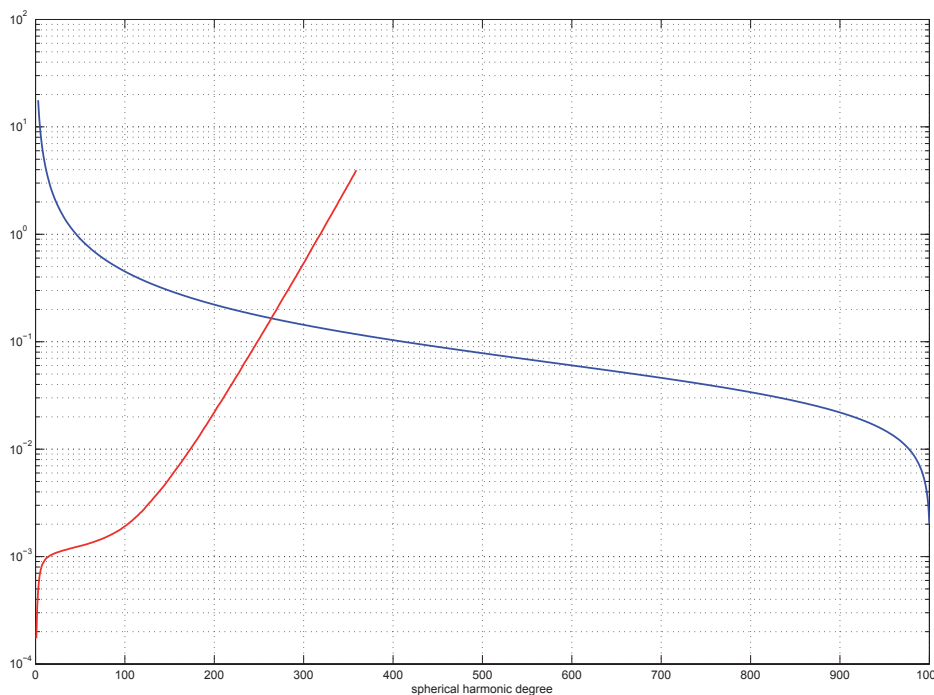

Figure 3.6: Cumulative commission error (blue line) for the GOCE model and omission error (red line) for the geoid undulation.
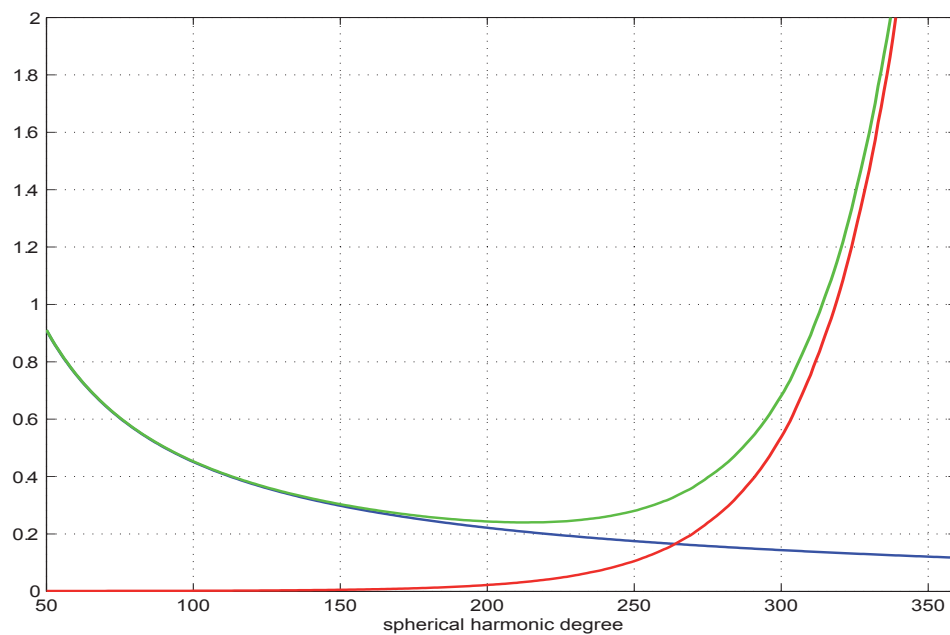

Figure 3.7: Cumulative commission error (blue line) for the GOCE model, omission error (red line) and global error (green line) in terms of the geoid undulation.

$$OM_L = \sqrt{\sum_{l=L+1}^{\infty} c_l}$$

(3.9)

To compute this error we have to know the degree variances up to infinite degrees, but, because of the rapid decrease of the signal degree variances, we can use, for instance, Kaula's rule (representing the expected signal size) up to $l = 1000$. Fig. 3.4 shows how the omission error varies when the degree L is varying in (3.9).

In Fig. 3.5 the spatial representation of the omission error is shown, computed using the ultra high resolution gravity field model EGM08. In this case the cut-off is at harmonic degree 45.

Fig. 3.6 shows the cumulative commission error, eq. (3.7) for the GOCE geopotential model, and the omission error, eq. (3.9), in terms of geoid undulations. We can observe that the omission error is dominant around up to degree $L = 265$. After this degree the cumulative commission error is greater than the omission component.

In Fig. 3.7 both the errors (commission and omission) are reported and their sum that represents the global error. With this simulation of the GOCE gravity field, the minimum of the global error is at $L = 215$.

So far the commission and omission errors are defined in the spectral domain, as functions of spherical harmonic degree. The same concepts can be defined in the spatial domain. We define the covariance function between
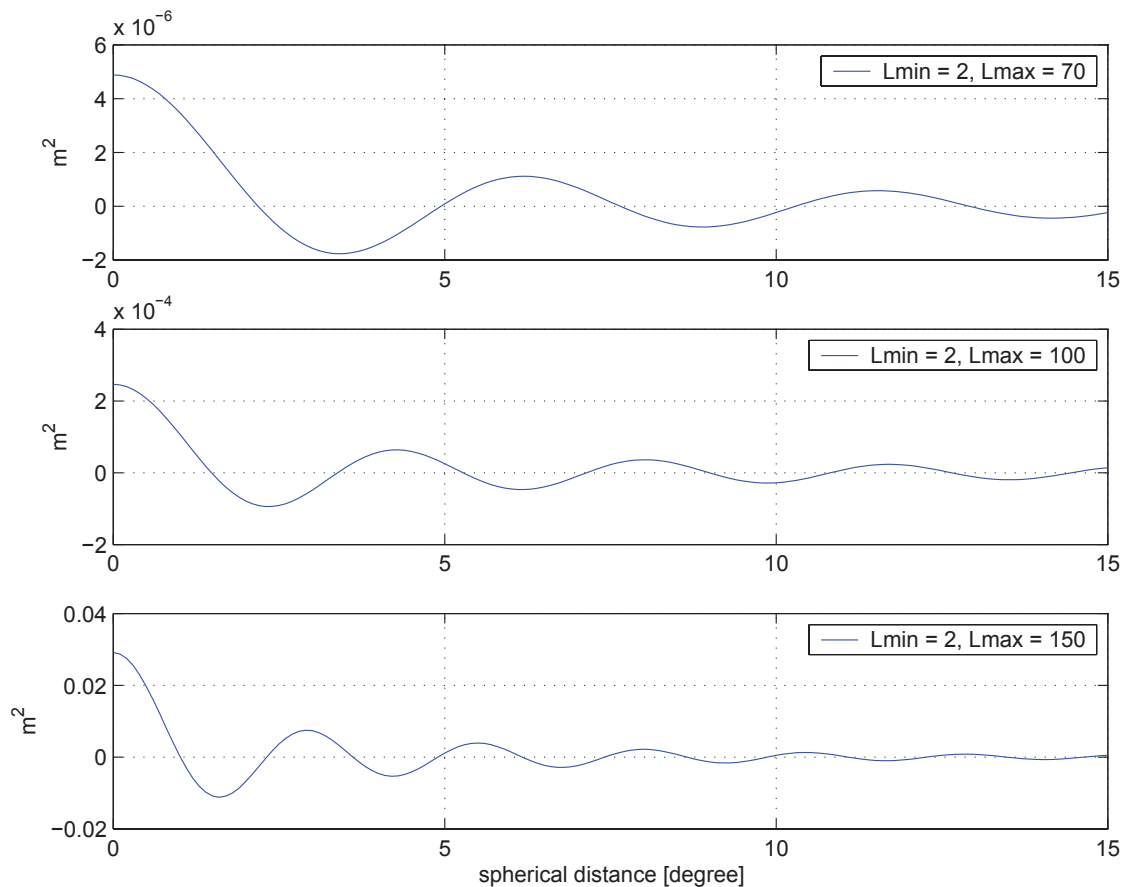

Figure 3.8: Covariance functions of the geoid undulation (EIGEN model) computed for different maximum degrees.

two points P and Q at spherical distance ψ as

$$C(\psi) = \sum_{l=0}^{L} c_l \, P_l(\cos \psi)$$

(3.10)

where c_1 are the degree variances of the degree l and P_l are the Legendre polynomials.

The error degree variances are the spectral representation of the errors of the gravity field. In the spatial domain they define the error covariance functions:

$$C_\varepsilon(\psi) = \sum_{l=0}^{L} \varepsilon_l \, P_l(\cos \psi) \quad .$$

(3.11)

The complete geoid error height covariance function between two points at a distance ψ is the sum of the commission and omission components

$$C_N^{(L)}(\psi) = R^2 C_\varepsilon(\psi) + R^2 \sum_{l=L+1}^{\infty} c_l^2 \, P_l(\cos \psi)$$

(3.12)

Also in this case it is appropriate to use the Kaula's rule to compute the omission error component.

In Fig. 3.8 three examples of commission error covariance functions (for the EIGEN geopotential model) for different maximum degrees L are shown.

We can observe that the length of correlation (i.e. the value of ψ for which $C(\psi)$ has decreased to half of its value at $\psi = 0$) decreases with increasing maximum degree, while the variance (i.e. the value of the covariance function in the origin) increases, see Table 3.1.
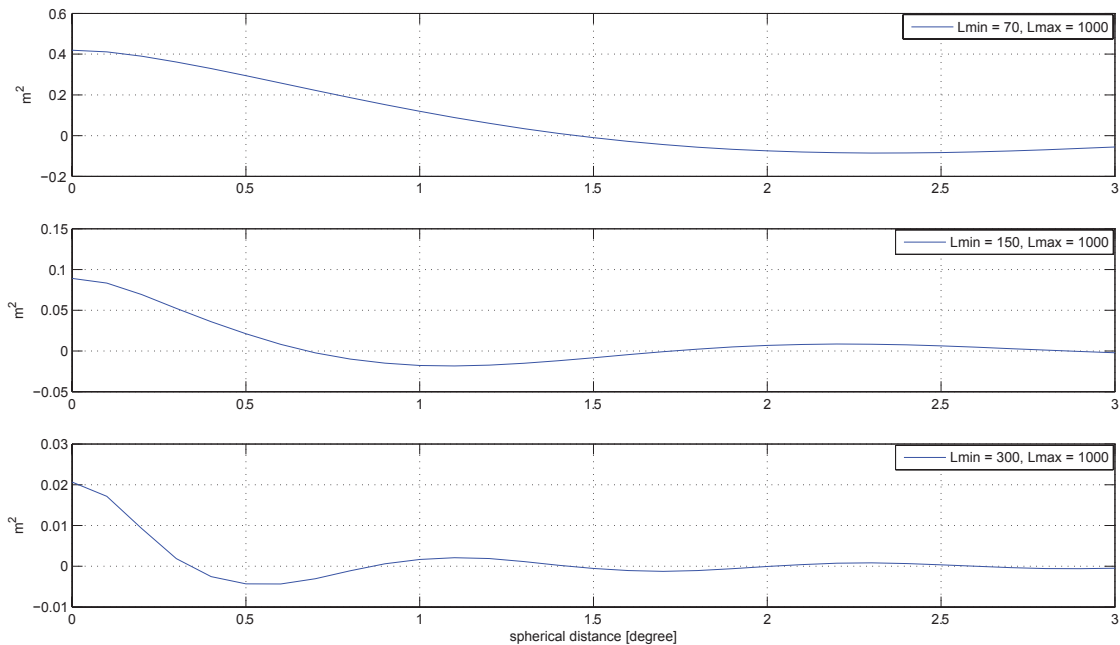

Figure 3.9: Covariance functions of the omission error for the geoid undulation computed for different maximum degrees

Table 3.1: Variance, RMS and length of correlation computed considering the covariance function of the EIGEN model, with different maximum degree.

	variance (m²)	RMS (m)	length correlation (°)
L = 70	$4.88 \cdot 10^{-6}$	0.0022	1.35
L = 100	$2.46 \cdot 10^{-4}$	0.0157	0.90
L = 150	0.0291	0.1707	0.65

Using the Kaula rule it is possible to compute the covariance function of the omission error. In Fig. 3.9 the omission error covariance functions are shown for different minimum degree L. Table 3.2 shows how in this case the variance decreases with increasing L. This corresponds to the fact that knowing the model with high resolution (up to high degree L), the un-modelled signal becomes smaller.

Table 3.2: Variance, RMS and length of correlation of the omission error for different minimum degree.

	variance (m²)	RMS (m)	length correlation (°)
L = 70	0.42	0.64	0.75
L = 150	0.09	0.30	0.45
L = 300	0.02	0.14	0.25

In the omission error covariance function, harmonic degrees from L to 1000 are contained. This approximately means that wavelengths corresponding to a spherical distance shorter than $\psi° = 360°/L$ are considered. This explains why the length of correlation decreases when L increases.

In all these considerations we assume a simplified situation, because we are consider the errors to be homogeneous and isotropic without taking into account the correlations between coefficients.

4 Filtering

The absolute sea surface topography ζ is the difference between the sea surface height (SSH) h relative to a reference ellipsoid (measured by satellite altimetry) and the geoid height N referred to the same ellipsoid:

$$\zeta = h - N$$

The geoid undulation is given as an expansion into spherical harmonic functions, (3.3).

The SSH h is derived from satellite altimetry. The measurements are given as point values profile-wise along foot-prints of the satellite tracks. By now a huge set of data from several altimetric missions is available, that constitutes the basis of the computation the SSH with high accuracy and precision.

The two components h and N have different resolutions. For the geoid the resolution is defined by the maximum degree L of the harmonic expansion (3.3). For the altimetric data the resolution is defined by the sample pattern in along-track and cross-track direction. We assume the geoid resolution always to be the limiting factor. For this reason we will remove all small scales from the altimetric data that are not resolved by the geoid. This synchronization of resolution may be achieved by applying the same low-pass filter to the altimetric data and to geoid undulation.

The concept of resolution is strictly related to the concept of mathematical representation of the data. For example, if we consider the geoid height and we use a spherical harmonic representation, it is easy to identify its different spectral components with the spherical harmonic degree and order. But for the sea surface height the spherical harmonic expansion is a priori not a suitable representation, because the data are confined to ocean areas.

The geoid undulation is a global quantity and it is naturally represented by spherical harmonic functions, that are also global, while the SSH is defined only in ocean areas and its spectral content is much higher.

Here we will analyze three approaches to solve this spectral inconsistency.

The first proposal is to expand the altimetric sea surface into the land areas. In this way the geoid and the sea surface have the same type of global spectral representation and they can be processed into a compatible form.

The second approach consists in the analysis in a local region, in which the data are considered disregarding their global characteristics.

The third approach consists in an analysis of the data along the profiles of the altimetric tracks (see chapter 5).

To remove the short wavelengths from the SSH, a low pass filter is needed. In this article we will analyze various types of filters for the global as well as for the local approach.

To check the accuracy of the proposed filters, we defined, for both approaches, a general procedure of simulation which is shown in Table 4.1. The differences between estimate and simulated surface give an indication of the properties of the filtering procedure.

In the follow we use the EIGEN model [1] up to degree L=180 to simulate the SSH on the oceans and we consider the threshold of the filter corresponding

to k_0=60.

The results of the global and the local approach will be compared in a limited box. The chosen area ($\varphi \in$ [–45°,–65°], $\lambda \in$ [40°W,20°E]) is compatible with the Atlantic sector of the Antarctic Circumpolar Current (ACC), see Fig. 4.1. We decided to consider this area because the ACC is an important feature of the deep ocean circulation; it transports and exchanges deep and intermediate water between the Atlantic, Indian and Pacific Ocean, and it contributes to the deep circulation in all basins. This current is a fundamental component in the models for the global climate of the Earth.

Table 4.1: Scheme of the simulation to check the accuracy of the filtering.

| 1.	Construction of a simulated SSH, with known spectral content, using geoid heights synthesized from a gravity model to a certain maximum degree L.
2.	Application of a filter (with threshold) on this surface function obtaining, if the filter works correctly, a filtered surface with spectral content, up to $k_0 < L$.
3.	Comparison between this filtered surface with the same surface obtained by direct spherical harmonic synthesis, using the same a-priori model up to k_0.
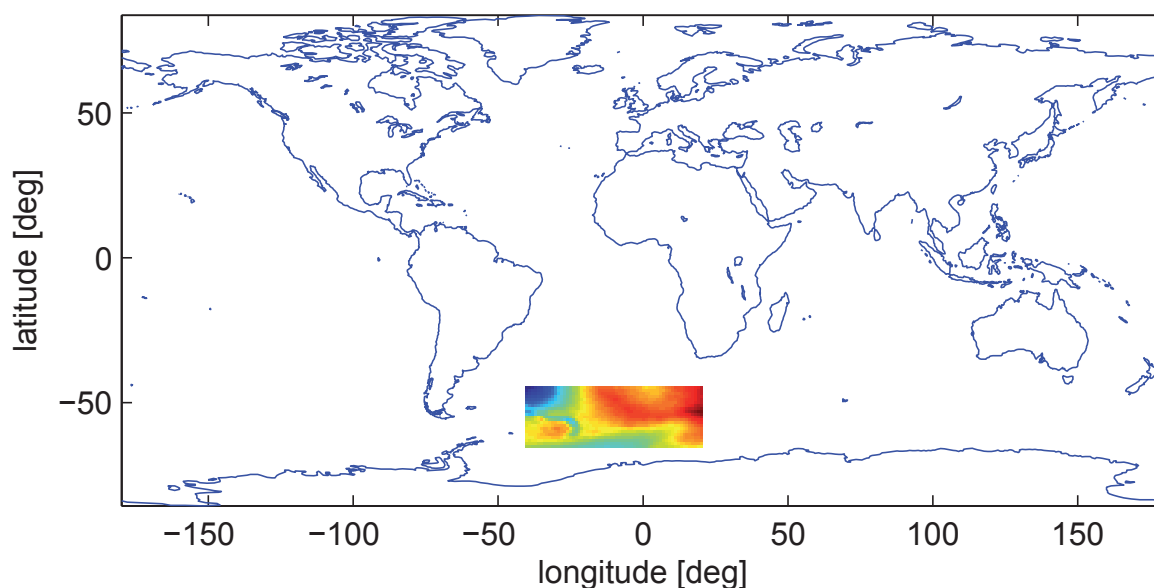
Figure 4.1: The area selected for this study.

4.1 From ocean only to global

Starting from the altimetric data, available only over the oceans, we want to derive from these ocean data a global altimetric sea surface that can be made compatible with the geoid surface.

The global altimetric sea surface will then be represented using spherical harmonic functions, (3.3). Then geoid and sea surface are given in the same type of spectral representation, i.e. spherical harmonics, and they can be processed (filtered) into a compatible form.

This procedure was developed in [Wang, 2007], where the following approaches of expanding and filtering the sea surface heights are tested over all oceanic surfaces.

In order to be able to expand altimetric data into a series of spherical harmonics, all land areas (and ocean data gaps) have to be filled with data as well.

We will illustrate different methods to achieve this. Then we analyze the performance of the different filters.

The simplest way to achieve a global surface is to complement the altimetric sea surface data by zero values on land. It is well known that the drawback will be very "unnatural" oscillations (Gibbs phenomenon) in the spherical harmonic representation along the borderline from altimetric data to zero values due to the sharp sea-to-land edge.

In order to reduce the strong discontinuity along the coastlines we fill the land with another geoid, namely EGM96, again up to degree L=180. We call this reconstructed global surface S_1. Of course, also in this case, a discontinuity along the coastlines is still present but much smaller.

It is necessary to reduce this discontinuity further, to make the input signal smooth enough for a spherical harmonic representation. The general idea is to generate a "transition zone" along the coastlines, on the land side in which a smooth transition to the ocean and land function will be attempted. Through interpolation there will be mixed data in the interpolation zone based on both ocean and land data. The global data set will then be divided into three parts (see Fig. 4.2): the geoid heights from EIGEN model on the ocean representing the altimetric surface (N^{180}_{ocean}), the geoid heights from EGM96 on land (N^{180}_{land}) and the interpolated data in the transition zone.

The transition zone is generated expanding the coastline polynomial towards the land direction. The size of the transition zone is arbitrarily fixed equal to 1.25°, but other choices may be considered as well.
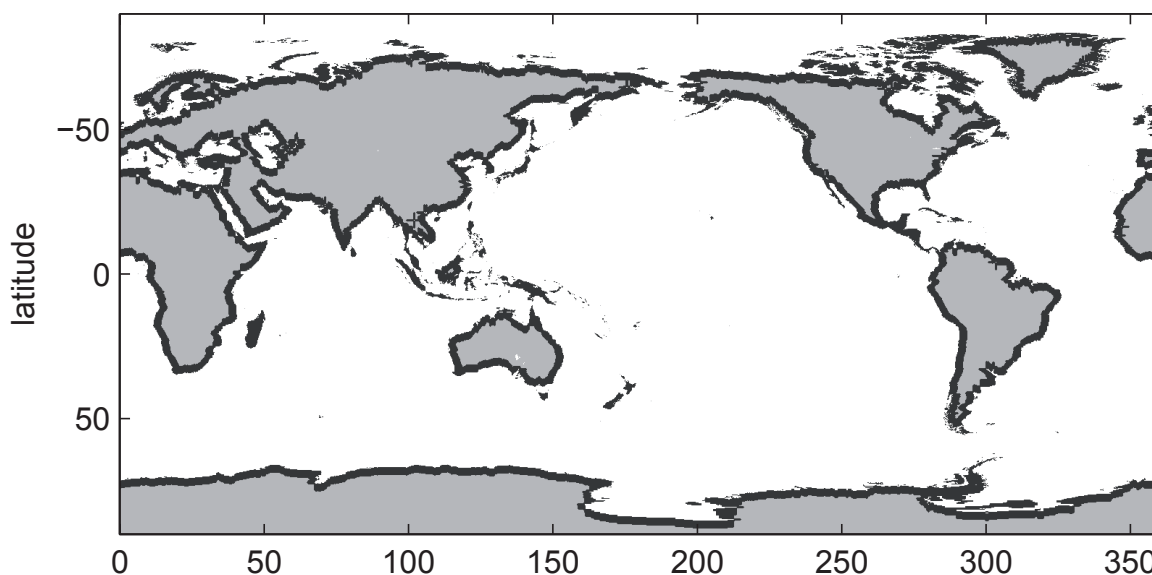

Figure 4.2: The division of the Earth's surface: ocean (white), land (grey) and transition zone along the coastline (black).

The data on the ocean and on land will be used to interpolate the data in the transition zone and the values in the interpolation zone will be replaced by the predictions.

To predict the values in the transition zone three methods will be tested:

- 2D polynomial interpolation;

- prediction by least squares collocation;

- *iterative procedure*.

After the prediction we have three surfaces that differ only in the transition area.

2D polynomial interpolation

The prediction in the transition zone is made using a 2D cubic interpolator (standard Matlab routine), based on the Delauny triangulation of the data. With this method all the data points are connected with triangles in such way that all the data are located at the corners of each triangle. If the point to be predicted is inside a triangle, the values at the three corners are used to compute the prediction value. If it is not inside any triangle, it is linked to the nearest triangle and then linearly interpolated.

We call the global surface reconstructed by polynomial interpolation S_2.

Interpolation by least squares collocation

An alternative method to perform the interpolation in the transition zone is the use of least squares collocation, [Moritz, 1980]. In this case, instead of simple polynomials, Legendre polynomials that are mathematically close to the global representation of the data in terms of associated spherical harmonics are used.

For computational reasons, we consider for each interpolation point Q of the transition zone a window with size 10°×10° and we use for the prediction all data (N^{180}_{ocean} and N^{180}_{land}) inside this window.

Using the prediction formula we can write for the interpolated value:

$$\tilde{N}_Q = C^T(\psi_{PQ}) \cdot (C(\psi_P) + D)^{-1} \begin{cases} N^{180}_{land} \\ N^{180}_{ocean} \end{cases} \tag{4.1}$$

where C is the isotropic, global covariance matrix of the geoid heights:

$$C(\psi_{PQ}) = R^2 \sum_{l=2}^{180} c_l P_l(\cos\psi_{PQ}) \tag{4.2}$$

depending only on the spherical distance ψ_{PQ}; c_l are the degree variances of an a-priori gravity model, namely

$$c_l = \sum_{m=-l}^{l} y_{lm}^2 \tag{4.3}$$

and P_l are the Legendre polynomials. D is the covariance matrix of the measurement errors and, in this preliminary study, it is assumed $D = 0$.

Eq. (4.1) contains the inversion of a full matrix. The dimensions of this matrix depend on the number of points used in the prediction. As consequence, it is necessary to consider only a limited area around each point of prediction. If for each prediction we consider $(r+1)(r+1)$ points, we must invert a full

matrix with size $(r+1)^2$ $(r+1)^2$. To determine the quantity r we can look at the behaviour of the covariance function involved in (4.1). In Fig.4.3 are shown the theoretical covariance functions computed using different minimum degrees.
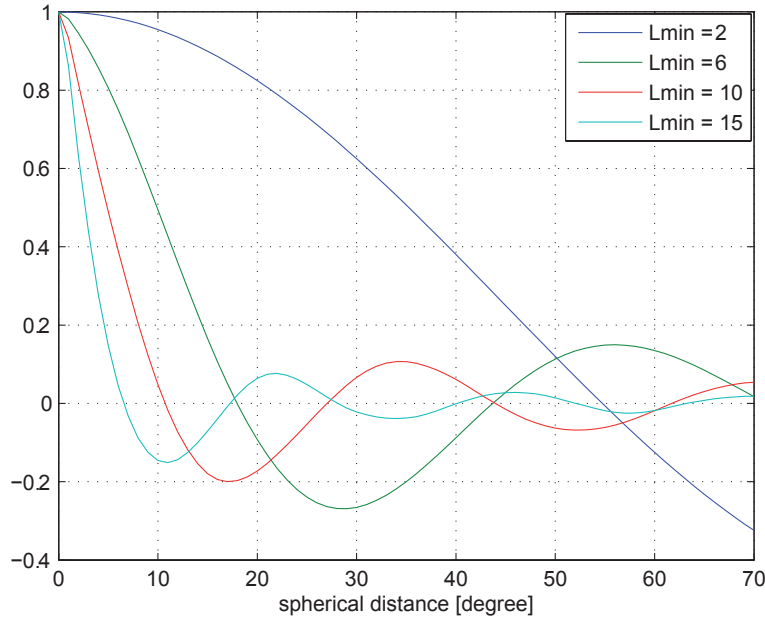

Figure 4.3: Normalized covariance functions computed using EGM96 with different minimum degrees.

If we consider a model starting from the minimum degree L_{min} = 2, the length of correlation is 35°, while using L_{min} = 10 we have a length of correlation of 5°. This means that, if we use for the prediction a model starting from L_{min} = 2, we must consider at least an area 35° x 35° around each point of the transition zone. Then it is necessary to invert a full matrix (1296 x 1296) for each point of prediction (for a grid with sampling of 1°) and this could be numerically heavy. We decided to choose the minimum degree equal to 10 and the corresponding local grid will be composed of 11 x 11 points.

To make the data compatible with this hypothesis, the synthesized values on land and ocean are computed using the corresponding geo-potential model with the same minimum degree (L_{min} =10). This is equivalent to assume that the a priori model is known up to this degree. This assumption could be reasonable for the first simulations.

Summarizing, the interpolation procedure works locally, using a window of 11 x 11 points moving over the complete area. We denote the obtained surface using the prediction by least squares collocation S_3.

Iterative approach

The last of our methods is based on a different approach, namely an *iterative procedure*.

The idea is proposed in [Gruber, 2000]. We start using initially the geoid to degree and order 180 on land from the EGM96 model (N^{180}_{land}) and the EIGEN geoid to the same degree and order on ocean (N^{180}_{ocean}) simulating the altimetric surface, without considering the transition zone.

Next we perform a global spherical harmonics analysis to get harmonic coef-

ficients and then perform a synthesis to come back to the geoid. After this process, we get a new "mixed geoid" on the globe. We keep the original EIGEN geoid to degree and order 180 on ocean, but on land we replace the EGM96 geoid by the derived "mixed geoid". Then we repeat this process. Because this "mixed geoid" on land is also affected by data from ocean, it will assimilate the ocean and land data so that the edge between land and ocean will become smaller and smaller. In this case, there is not a transition zone like in the previous paragraphs.

We call the surface obtained with this approach S_4.

4.1.1 Filtering in the global approach

Summarizing we have now four global surfaces, see Table 4.2, that can be represented with a spherical harmonic expansion and then filtered up to the selected harmonic degree.

Table 4.2: Different considered global surfaces.

surface	ocean	transition zone	land
S_1	EIGEN	--	EGM96
S_2	EIGEN	polynomial interpolation	EGM96
S_3	EIGEN	prediction by least squares collocation	EGM96
S_4	EIGEN	--	mixed geoid (smooth transition)

The filtering process in the spectral domain is a multiplication of the spherical harmonic coefficients with a spectral weight W_l:

$$\tilde{N}(P) = R \sum_{l=2}^{L} \sum_{m=-l}^{l} W_l \, y_{lm} Y_{lm}(P) \tag{4.4}$$

The spherical harmonic coefficients are weighted by W_l, which can be calculated through

$$W_l = \int_0^\pi W(\alpha) P_l(\cos \alpha) \sin \alpha \, d\alpha \tag{4.5}$$

where $W(\alpha)$ is an isotropic weighting function on the sphere that is only dependent on the spherical distance α.

To filter the high frequencies (from k_0+1 to L) of our surfaces we propose two filters: the direct cut-off and the "Gauss" shape filter.

 Direct cut-off filter. The direct cut-off filter up to k_0, or ideal low pass filter, consists in choosing as maximum degree L = k_0 in (4.4). An ideal low-pass filter completely eliminates all spectral content above the cut-off degree. The coefficients below will pass unchanged.

Starting from a global surface S, by spherical harmonic analysis, it is possible to compute the corresponding spherical harmonic coefficients y_{lm} up to a certain harmonic degree related to the grid size.

To obtain the surface containing the frequencies up to k_0, we consider:

$$\tilde{N}^{k_0}(P) = R \sum_{l=2}^{k_0} \sum_{m=-l}^{l} y_{lm} Y_{lm}(P)$$

that corresponds to spectral weights

$$W_l = \begin{cases} 1 & l \le k_0 \\ 0 & l > k_0 \end{cases}$$

in (4.4).

Gauss shape filter. An alternative is to consider a Gauss filter. The Gauss filter corresponds to a Gaussian function

$$G(x,y) = \frac{1}{2\pi\sigma^2} e^{\frac{x^2+y^2}{2\sigma^2}}$$

with a similar shape in space and spectral domain, with the standard deviation of the distribution σ related to the threshold of the filter. The Gauss filter corresponds to a cap with a certain spherical radius α_r in the space domain.

The formula for the weighting function W_l for the Gauss filter is defined in [Jekeli, 1981] and improved by [Wahr et al., 1998]. It can be computed by recursive formulas:

$$W_0 = 1, \quad W_1 = \left[\frac{1+e^{-2b}}{1-e^{-2b}} - \frac{1}{b}\right], \quad \cdots \quad W_l = -\frac{2l-1}{b} W_{l-1} + W_{l-2} \tag{4.6}$$

where

$$b = \frac{\ln(2)}{1-\cos\alpha_r}.$$

The radius α_r is empirically related to the degree k_0 [Zenner, 2006]:

$$\alpha_r \cong \frac{1.45 \cdot 10^4}{k_0} \tag{4.7}$$

The maximum degree 60 corresponds roughly to $\alpha_r = 250$ km.

Also quite different from the ideal low-pass filter at degree and order 60, the Gauss filter will take, with low weight, coefficients up to degree and order 120 [Zenner, 2006]. Each degree and order will be weighted correspondingly.

4.1.2 Results of the global approach

Following the scheme of Table 4.1, we compare the differences between the simulated (N^{60}) and the filtered geoid undulation ($\tilde{N}^{60}$) over all oceanic surfaces and in the considered ocean box ($\varphi \in [-45°,-65°]$, $\lambda \in [40°W,20°E]$).

Fig. 4.4 and Fig. 4.5 show the results for the four surfaces described in the previous section on the oceans, considering the direct cut-off filter (Fig. 4.4) and the Gauss filter (4.5).

In both cases the stronger deviations occur near the coastlines. The direct

cut-off filtering produces a clearer ringing effect as compared to the "Gauss" filter.

The statistics of the differences over all the oceans are reported in Table 4.3.

Table 4.3: Statistics of the differences between simulated (N^{60}) and filtered ($\bar{N}^{60}$) geoid undulation on the oceans. The units are meters.

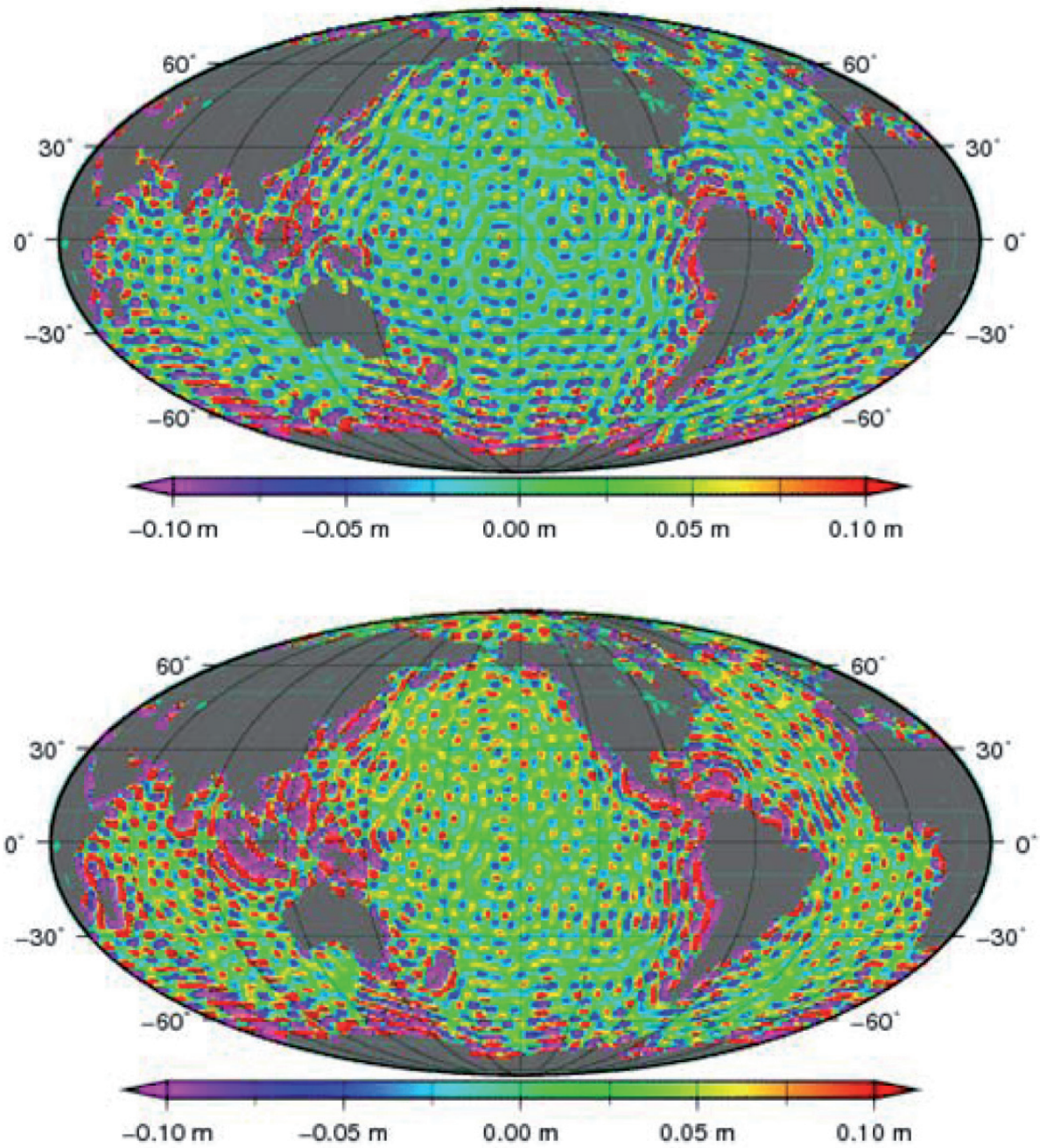|	Mean	st.dev.	max	min
S_1 cut-off	+0.0260	0.1173	2.8681	−1.3279
S_2 cut-off	+0.1320	0.1308	2.4232	−2.2833
S_3 cut-off	−0.0029	0.1684	3.1237	−1.3821
S_4 cut-off	$5.3 \cdot 10^{-4}$	0.0865	2.3606	−1.2132
S_1 Gauss	0.0023	0.0476	1.2994	−0.7129
S_2 Gauss	0.0106	0.0684	1.0699	−1.1493
S_3 Gauss	−0.0025	0.0709	1.4202	−0.7000
S_4 Gauss	$−6.6 \cdot 10^{-5}$	0.0330	1.0444	−0.5798

Figure 4.4-a: Differences between simulated (N^{60}) and direct cut-off filtered ($\tilde{N}^{60}$) geoid undulations on the oceans. The surface S_1 is considered in the upper panel and S_2 in the lower one. The units are meters.
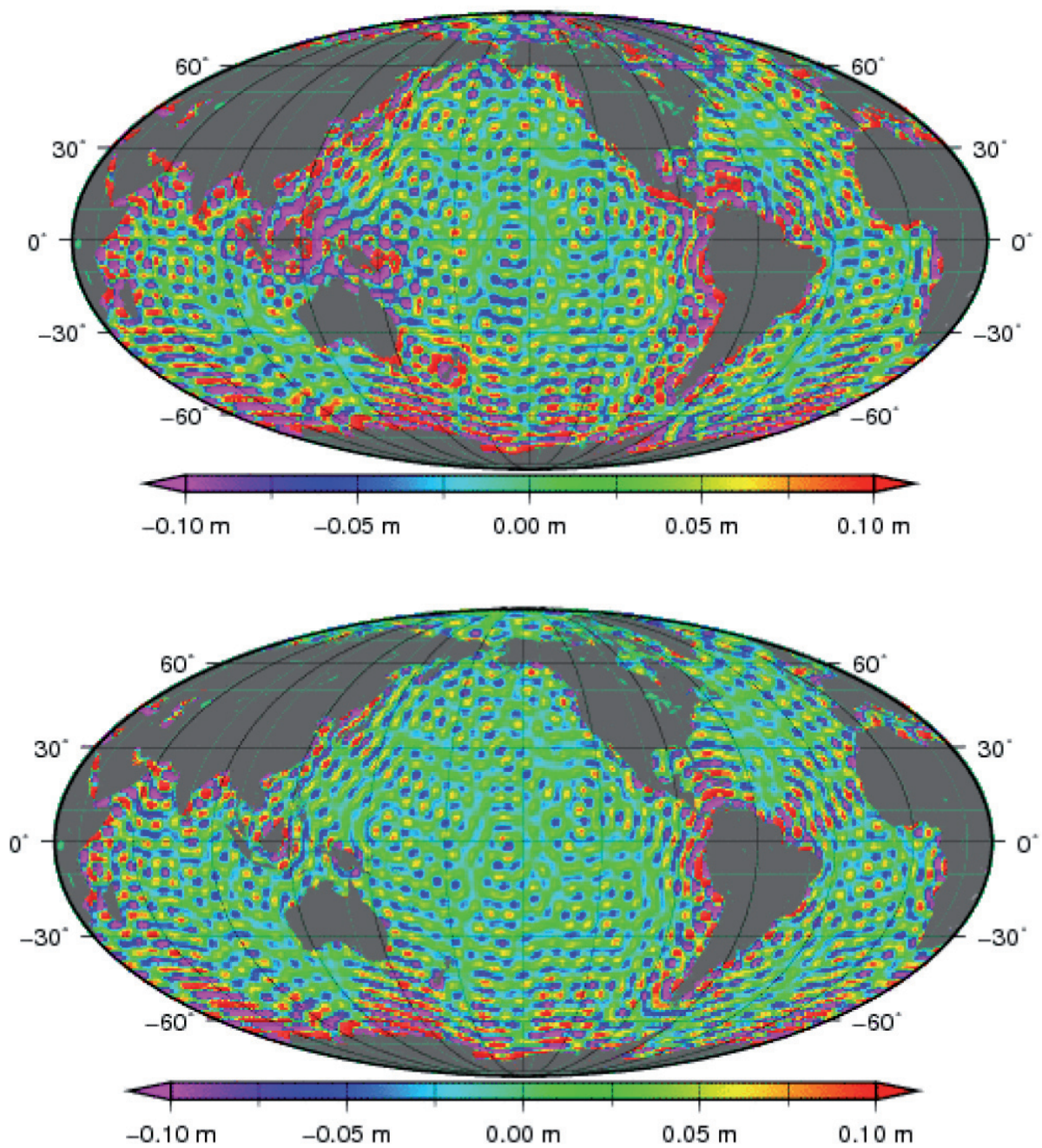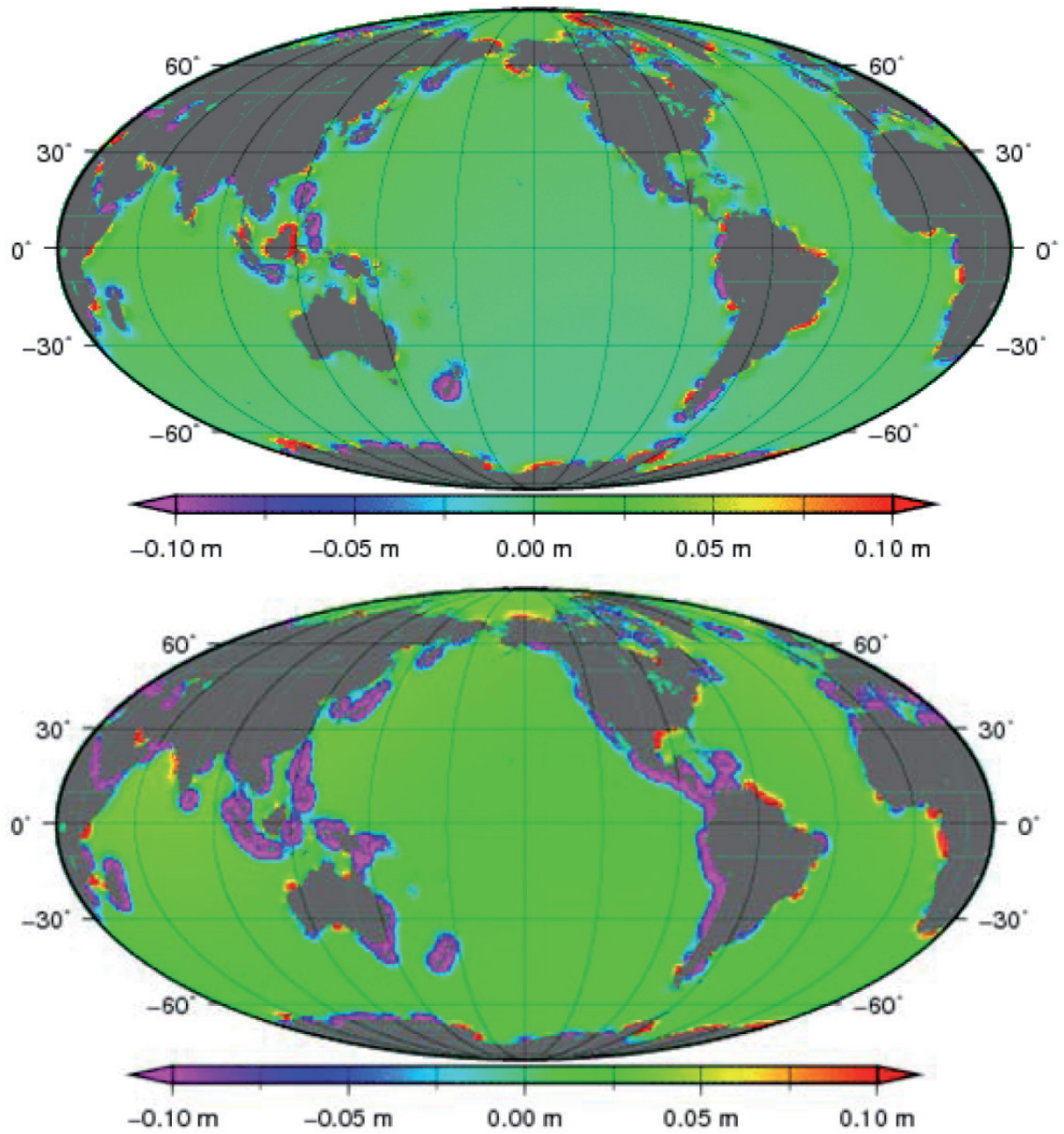
Figure 4.4-b: Differences between simulated (N^{60}) and direct cut-off filtered ($\hat{N}^{60}$) geoid undulations on the oceans. The surface S_3 is considered in the upper panel and S_4 in the lower one. The units are meters.

Figure 4.5-a: Differences between simulated (N^{60}) and "Gauss" filtered ($\bar{N}^{60}$) geoid undulations on the oceans. The surface S_1 is considered in the upper panel and S_2 in the lower one. The units are meters.
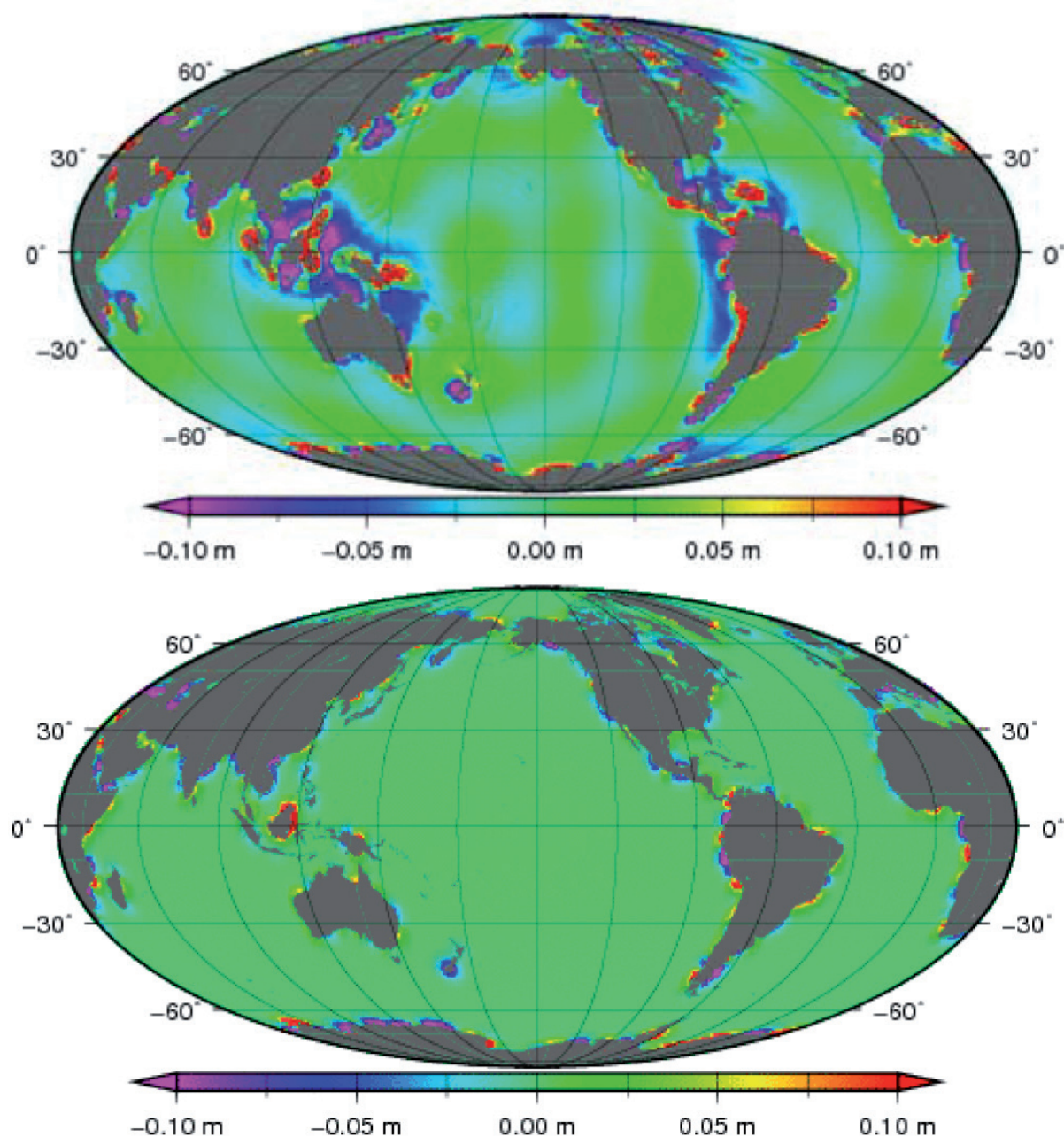
Figure 4.5-b: Differences between simulated (N^{60}) and "Gauss" filtered ($\tilde{N}^{60}$) geoid undulations on the oceans. The surface S_3 is considered in the upper panel and S_4 in the lower one. The units are meters.

As expected the results obtained with the Gauss filter are better than the results of the direct cut-off filtering.

The filtering of the surface S_3, corresponding to the prediction in the transition zone made by least squares collocation, shows biggest residuals when compared to the others surfaces. This could be due to the limited window used for the prediction. The data are well distributed around each prediction point, but obviously not sufficiently distant. This needs further investigations.

Another disappointing result is that the analysis using the surface S_1 is more

accurate than the analysis using the surface S_2. As is shown in [Wang, 2007] the simple polynomial interpolation in the transition zone is not able to reduce the discontinuities along the coastline and this can also introduce further discontinuities instead of reducing it.

The smoothing of the discontinuities along the coastline made by the iterative procedure (surface S_4) allows a filtering procedure with a global accuracy of only 3 cm.

The results are essentially the same as those obtained in [Wang, 2007].

The selected ocean box ($\varphi \in [-45°,-65°]$, $\lambda \in [40°W,20°E]$) is sufficiently far from the coastlines. Thus here the results are better for both filtering procedures, as is shown in Fig. 4.6 and Fig. 4.7. In Fig. 4.6 (direct cut-off filtering) Gibbs effects are visible, while in Fig. 4.7 (Gauss filtering) they are successfully reduced.

In Table 4.4 the statistics of these differences between simulated and filtered surfaces are shown considering only the points of the ocean box.

The iterative procedure (surface S_4) gives definitely better results compared to the interpolation (surfaces S_2 and S_3), reaching high accuracy.

In [Albertella and Rummel, 2008] the effects of the extension of the sea surface to the land areas are studied by means a one-dimensional example. Here it is shown that the introduced discontinuity produces errors localized near the discontinuity itself and that they quickly decrease with growing distance from this point.

The results obtained with the surfaces S_1 and S_4 (that do not involve the transition zone) are the same for different grid samplings (like for example 0.25°×0.25° instead of 1°×1°).

For the surfaces S_2 and S_3, on the contrary, the situation is different. If we change the grid resolution from 0.25°×0.25° to 1°×1° (as it is necessary for S_3 for numerical computation reasons) we also have to enlarge the transition zone. In this way, the grid resolution and the transition zone become comparable. Therefore for the surface S_3, we considered a 1°×1° grid and a transition zone 5 units wide, that means a distance of about 5°.

Tables 4.3 and 4.4 report the results corresponding to these cases. If we consider the same grid (1°×1°) and the same transition zone (~5°), also in the computation of surface S_2 we obtain a clear deterioration of the results. As is emphasized in [Wang, 2007] the Matlab polynomial interpolator does not work correctly and it introduces new discontinuities along the coastlines, instead of reducing them. This behaviour is getting worse when the ratio between the prediction and data points increases.

We can conclude that the global approach of filtering gives excellent results in case of the Gauss filtering when a global surface is created using the iterative procedure. In any case it must be observed that the results are good only at sufficient distance from the coastal areas.
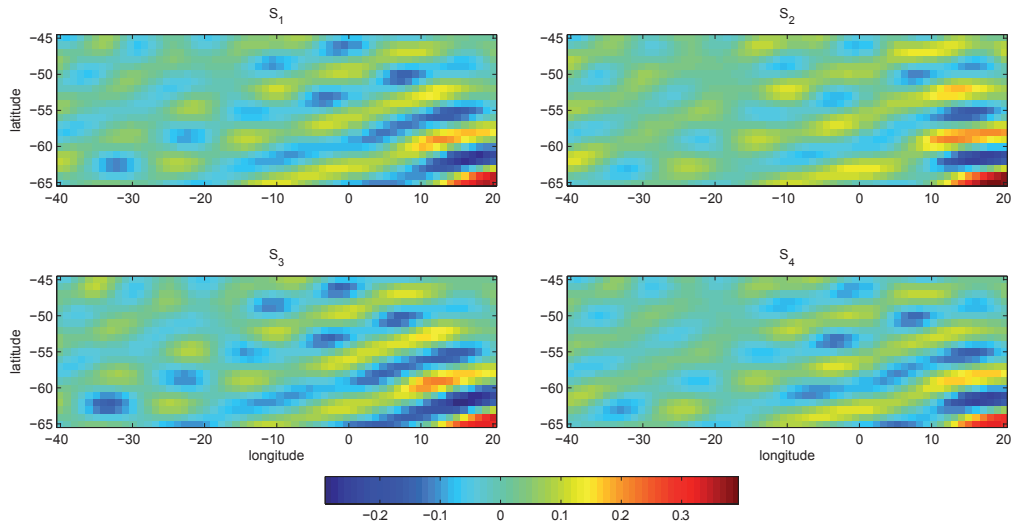
Figure 4.6: Differences between simulated (N^{60}) and direct cut-off filtered ($\hat{N}^{60}$) geoid undulation in the box ($\varphi \in [-45°,-65°]$, $\lambda \in [40°W, 20°E]$), considering the different global surfaces of Table 4.2. The units are meters.

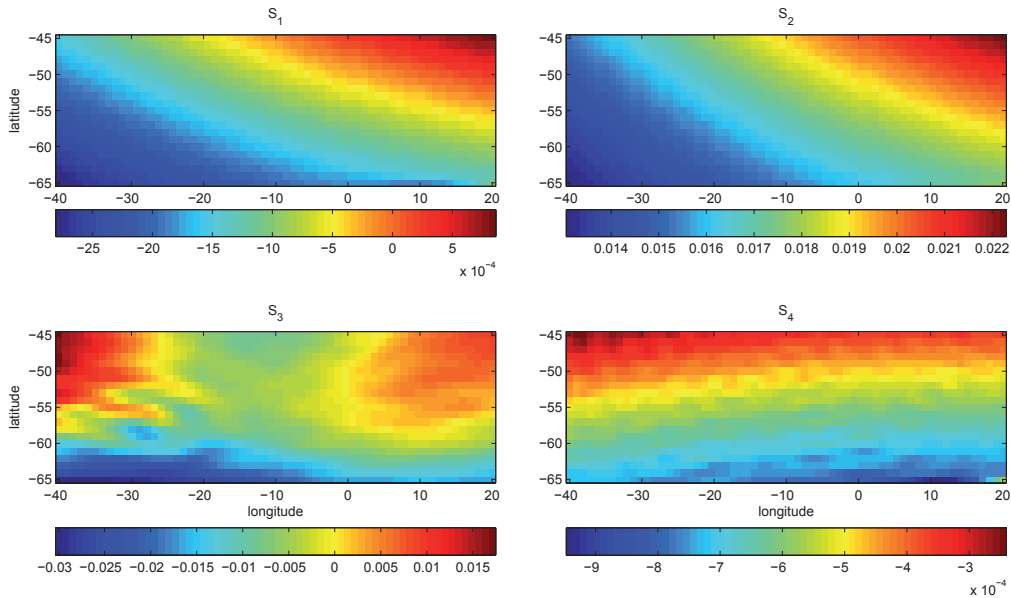*Figure 4.7: Differences between simulated (N^{60}) and "Gauss" filtered ($\hat{N}^{60}$) geoid undulation in the box ($\varphi \in [-45°,-65°]$, $\lambda \in [40°W, 20°E]$), considering the different global surfaces of Table 4.2. The units are meters.*

Table 4.4: Statistics of the differences between simulated (N^{60}) and filtered ($\hat{N}^{60}$) geoid undulation in the box ($\varphi \in [-45°,-65°]$, $\lambda \in [40°W, 20°E]$). The units are meters.

		mean	st.dev.	max	min
S_1	cut-off	$9.7 \cdot 10^{-5}$	0.0731	0.3515	-0.2746
S_2	cut-off	+0.0200	0.0712	0.3940	-0.2560
S_3	cut-off	-0.0040	0.0764	0.3300	-0.2908
S_4	cut-off	+0.0013	0.0665	0.3275	-0.2525
S_1	Gauss	-0.0011	$7.9 \cdot 10^{-4}$	$8.6 \cdot 10^{-4}$	-0.0028
S_2	Gauss	0.0171	0.0020	0.0223	-0.0131
S_3	Gauss	-0.0040	0.0092	0.0175	-0.0303
S_4	Gauss	$-5.6 \cdot 10^{-4}$	$1.4 \cdot 10^{-4}$	$-2.4 \cdot 10^{-4}$	$-9.4 \cdot 10^{-4}$

4.2 From global to local

An opposite point of view is to consider the issue of spectral compatibility as a local problem. In this case we consider an area on the ocean, in which we filter the SSH, using a local representation of the data.

In a limited area, a common spectral representation is a 2D Fourier representation, not only because it is adaptable to a limited area, but also because of its simplicity of the filtering operation in the spectral domain. Obviously we are assuming implicitly that the data are periodically continued in the area around our box.

In this section the use of the least squares collocation to estimate the low spectral components is studied as well.

4.2.1 Local 2D Fourier analysis

We consider the simulated SSH at the discrete points of the regular grid defined in our test area ($\varphi \in$ [–45°,–65°], $\lambda \in$ [40°W,20°E]). The sampling intervals are $\delta\varphi$= 0.5°, $\delta\lambda$ = 0.5° and M, N are the number of points along φ and λ-direction.

This function can be represented as a finite linear combination:

$$f(\varphi_k, \lambda_l) = \sum_{i=0}^{M-1} \sum_{j=0}^{N-1} F(u_i, v_j) \exp\left[2\pi i \left(u_i \varphi_k + v_j \lambda_l \right) \right]$$

(4.8)

where

$$F(u_i, v_j) = \frac{1}{MN} \sum_{k=0}^{M-1} \sum_{l=0}^{N-1} f(\varphi_k, \lambda_l) \exp\left[-2\pi i \left(u_i \varphi_k + v_j \lambda_l \right) \right]$$

(4.9)

Eq. (4.9) is the 2D Discrete Fourier Transform F of the discrete function f, u_i and v_j represent the longitudinal and the latitudinal component of the frequency and φ_k and λ_l are the sampling points. In the following, with a simplified notation we put $(u,v) \equiv (u_i, v_j)$ and $(\varphi, \lambda) \equiv (\varphi_k, \lambda_l)$.

It is well known, any filtering by convolution in the spatial domain, corresponds to a multiplication between the 2D Fourier Transform and the filter H in the spectral domain:

$$\overline{f}(\varphi, \lambda) = f(\varphi, \lambda) \otimes h(\varphi, \lambda) \Leftrightarrow \overline{F}(u, v) = F(u, v) \cdot H(u, v)$$

(4.10)

To check the filtering procedure we follow the scheme of simulation described in Table 4.1.

Again we apply first the ideal 2D low-pass filter (see Fig. 4.8 upper panel), that is defined for the cut-off frequency k_0, as:

$$H(u, v) = \begin{cases} 1 & \sqrt{u^2 + v^2} \leq k_0 \\ 0 & \sqrt{u^2 + v^2} > k_0 \end{cases}.$$

The well known drawback of this filter function is a ringing effect which occurs along the edges of the filtered real domain function.

Better results can be achieved with a 2D Butterworth low-pass filter, (Fig. 4.8 lower panel). The advantage is that the Butterworth filter has the same shape

in space and frequency domain and therefore the ringing effect is reduced. It is defined as:

$$H(u,v) = \frac{1}{1 + \left[\left(\dfrac{u}{a} \right)^2 + \left(\dfrac{v}{b} \right)^2 \right]^n}$$

(4.11)

where the index n controls the smoothing of the transition from 1 to 0 (see Fig. 4.8 (c)).
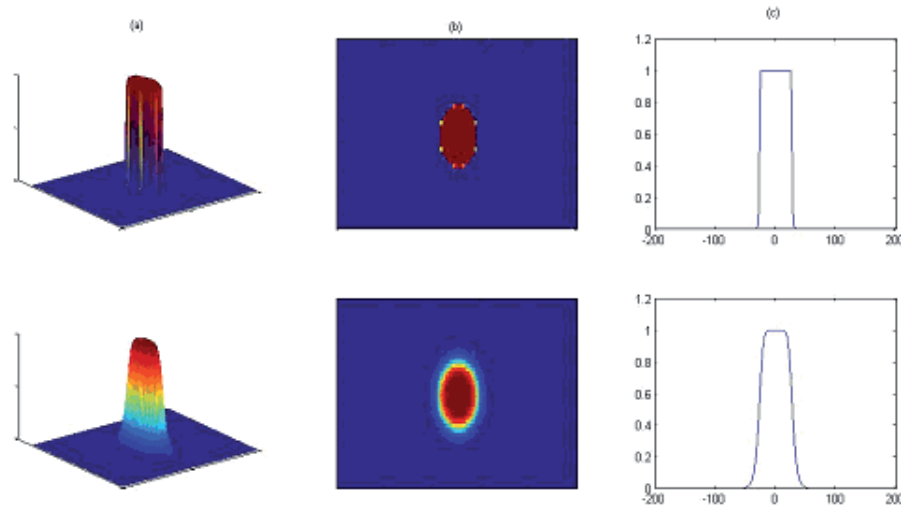

Figure 4.8: Ideal low-pass filter (top) and Butterworth low-pass filter (down) in the frequency domain. (a) 3D view; (b) view of the filters from top; (c) cross sections.

The two quantities a and b, semi-axis of the filter, are related to the cut off degree k_0 and to the dimensions of the box containing the data ($\Delta\varphi$, $\Delta\lambda$):

$$a = k_0 \frac{\Delta\varphi}{\pi}, \quad b = k_0 \frac{\Delta\lambda}{2\pi} \cos\varphi_m$$

(4.12)

where φ_m is the mean latitude of our test area: $\varphi_m = -55°$.

This filter is anisotropic. The axis b depends on the latitude of the considered area and the shape of the spectrum depends on the geographical position.

Fig. 4.9 shows the spectra of the same function N^{60} (geoid heights synthesized up to degree 60) in a box with fixed dimensions ($\Delta\varphi=20°$ $\Delta\lambda=60°$), but centred at different latitudes. One semi-axis is not varying, the second one is varying like $\cos\varphi_m$.

Starting from the simulated SSH (N^{180}), containing all the frequencies up to degree 180, we want to recover only the components with low spectral content (N^{60}).
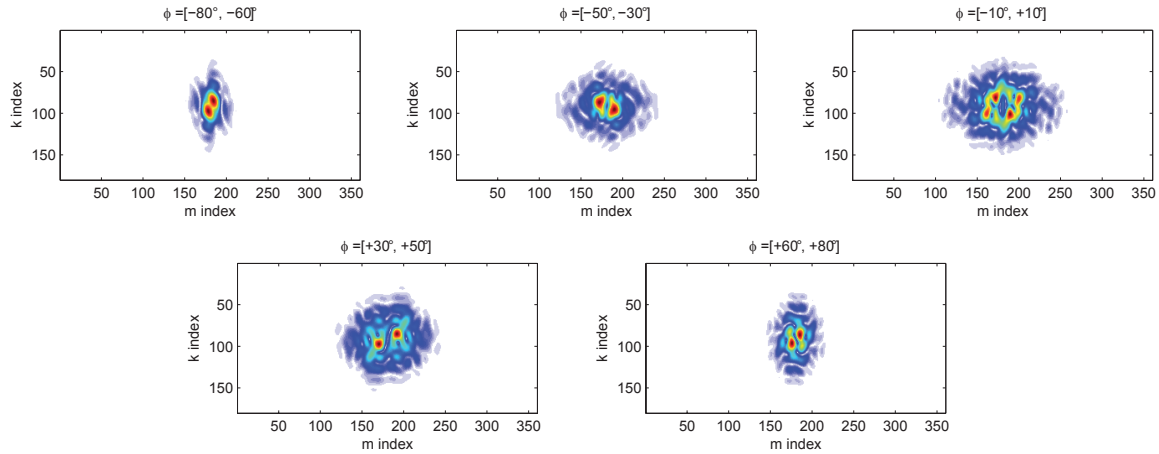
Figure 4.9: 2D Fourier spectra of the geoids heights (up degree 60) in different geographical positions. The longitude is constant $\Delta\lambda = [40°\text{W}, 20°\text{E}]$ *. The latitude is varying. The semi-axis b, the axis along the direction of the m index, varies as* $\cos\varphi_m$ *.*

Inspecting the shape of the Fourier spectra of the functions N^{180} and N^{60} (upper panel of Fig. 4.10) one observes that a simple low pass filter it is not adequate to reconstruct N^{60} with sufficient precision. In fact, the spectrum of N^{60} after the threshold corresponding to 60 (dashed line in the Fig. 4.10) does not drop to zero immediately but with a smoothed behaviour.

The problem could be solved by adding to the filtered spectrum a component computed using an a-priori model, for example the model EGM96. In this way the behaviour of the filtered function is made really close to the target function, (as is shown in the lower panel of Fig. 4.10).

The filtered function $\tilde{N}$ is obtained as:

$$\tilde{N} = h_{LP} \otimes N^{180} + h_{HP} \otimes N^{60} \tag{4.13}$$

where:

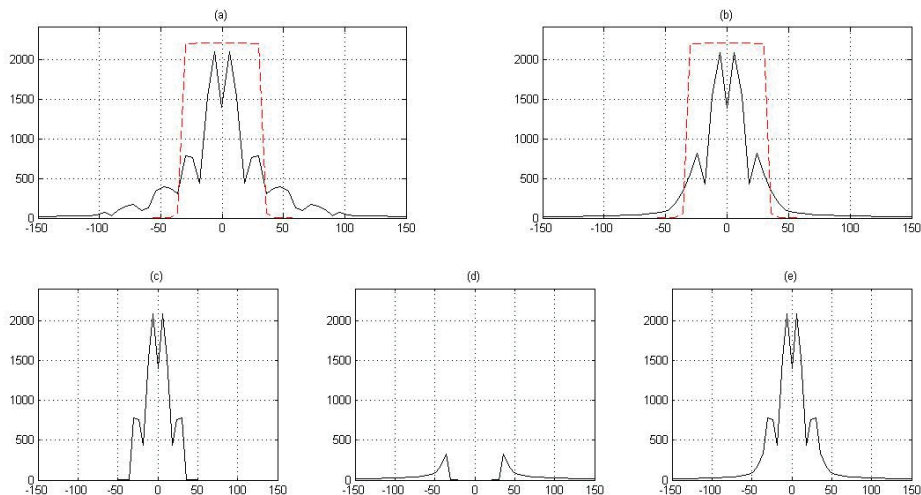- h_{LP} is the 2D low-pass Butterworth filter, with threshold 60;

Figure 4.10: Sections of the spectra of N^{180} *(a) and* N^{60} *(b) compared with the shape of the filter (dashed line). In the lower panel the scheme of the filtering procedure is shown: the low pass filter applied to* N^{180} *(c) is not adequate; it is necessary to add a component (d) computed using an a-priori model, in order to obtain an optimal result (e).*

- h_{HP} is the 2D high-pass Butterworth filter, with threshold 60;
- N^{180} is the geoid undulation synthesized up to 180 (which plays here the role of the SST);
- N^{60} is the geoid undulation synthesized up to 60 (taken from an a priori model).

First, the values of geoid undulations are generated on a spherical equiangular grid with coordinates $\varphi \in [-75°, -35°]$, $\lambda \in [70°W, 50°E]$. Over these data a filter (Tukey window) is applied. The larger area is introduced in order to smooth the values along the boundaries, as is shown in Fig. 4.11.

The area in which the filter is evaluated corresponds only to the inner part: $\varphi \in [-65°, -45°]$, $\lambda \in [40°W, 20°E]$.

Following the scheme of Table 4.1 in each point of the grid the geoid undulation is simulated using the EIGEN gravity model up to degree 180. Filter (4.13) is applied in the larger area and the resulting values $\tilde{N}$ are compared in the inner area with the geoid undulations N^{60} synthesized (always using the EIGEN model) on the same grid up to degree 60.

In Table 4.5 the statistics of the differences $d = \tilde{N} - N^{60}$ are reported. The precision of the filtering operation is around 3 cm.

Table 4.5: Statistics of differences between (N^{60}) and ($\tilde{N}^{60}$), filtered using the 2D Butterworth filter. The units are metres.

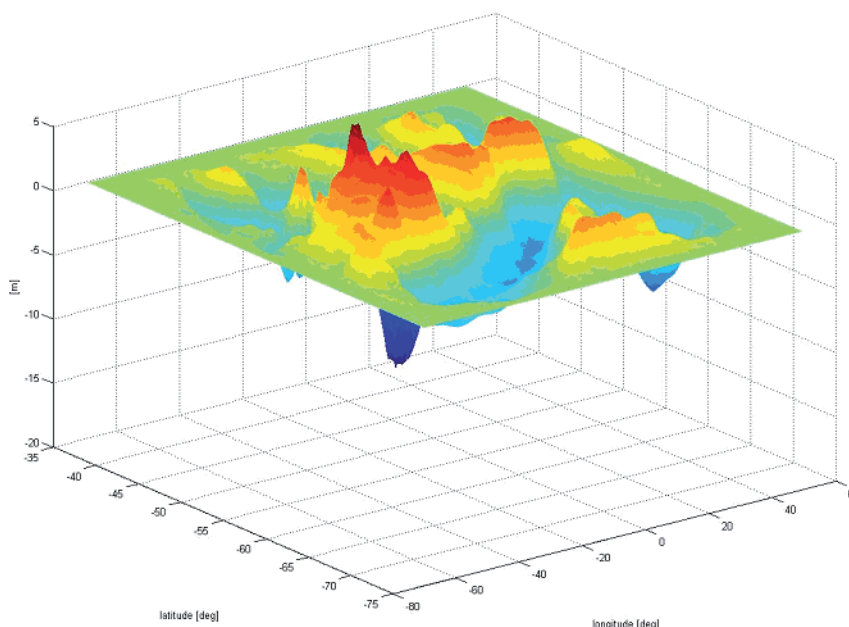| n° points	mean	st.dev.	max	min
4800	0.0016	0.0274	0.0826	−0.962

Figure 4.11: Geoid undulations up to degree 180 after the application of the Tukey filter to smooth the transition on the boundaries of the test area.

4.2.2 Local least squares prediction (collocation approach)

An alternative approach of selection of the low part of the spectrum is the use of the method of least squares collocation. If the covariance function is known, starting from observations of some functional of the gravity field, collocation can be used to predict the same functional in a different set of points.

We have

$$\tilde{N}_Q = C^T(\psi_{PQ}) \cdot (C(\psi_{PP}) + D)^{-1} \cdot N_P \tag{4.14}$$

where P are the grid points where the geoid undulation N_P is observed, Q are the points in which we want to compute it, $C(\psi_{PQ})$ is the covariance function of the geoid undulation (4.2) depending only on the distance between P and Q.

In [Brajovic, 2005] it is proposed the use of this method to separate the contribution of the low (L) and high (H) degrees in the same function. The covariance function (4.2) can be divided in two components:

$$C_N(\psi) = C^L + C^H = R^2 \sum_{l=2}^{k_0} c_l \cdot P_l(\cos\psi) + R^2 \sum_{l=k_0+1}^{L_{max}} c_l \cdot P_l(\cos\psi) \tag{4.15}$$

Starting from a set of geoid heights N_P, using (4.15) we can write

$$\begin{aligned}
\tilde{N}_P = \tilde{N}^L + \tilde{N}^H &= (C^L + C^H)^T \cdot (C + D)^{-1} \cdot N_P = \\
&= (C^L)^T \cdot (C + D)^{-1} \cdot N_P + (C^H)^T \cdot (C + D)^{-1} \cdot N_P
\end{aligned} \tag{4.16}$$

The estimated $\tilde{N}^L$ contains only the frequencies up to k_0 and $\tilde{N}^H$ contains only the frequencies from k_0+1 to L_{max}; this is exactly a definition of a low (or high) pass filter.

In this first analysis the noise is not considered (D=0) and for computational reasons, we consider a sampling interval equal to 1°.

The estimate of the components containing only the frequencies up to k_0=60 is

$$\tilde{N}^{60}(P_i) = (C^L)^T \cdot (C^L + C^H)^{-1} \cdot N^{180}(P_i) \tag{4.17}$$

where P_i are the points of our considered grid.

The quantity $\tilde{N}^{60}(P_i)$ is compared with $N^{60}(P_i)$

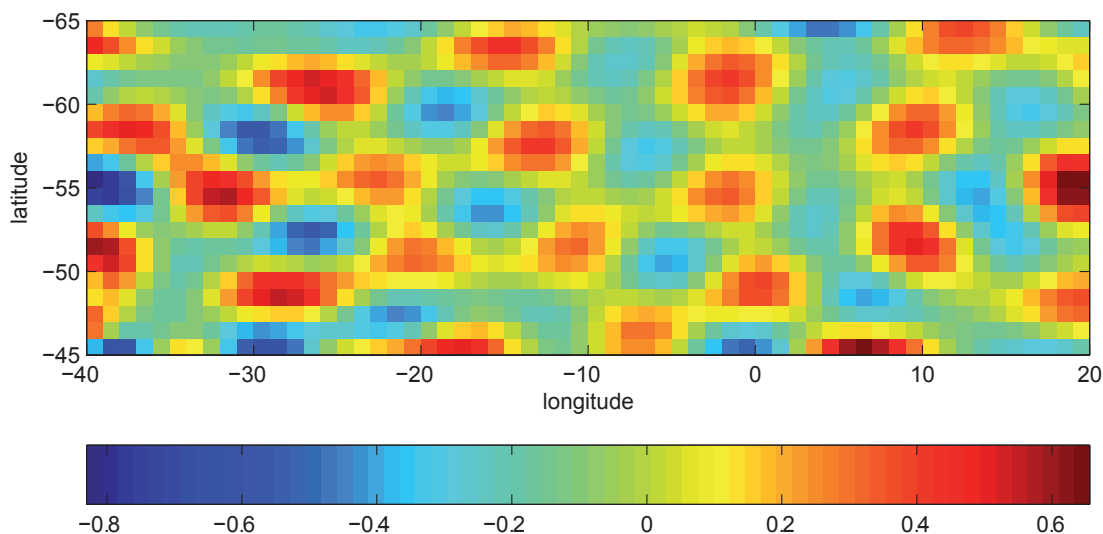$$N^{60}(P_i) = R \sum_{n=2}^{60} \sum_{m=-n}^{n} y_{nm} Y_{nm}(P_i)$$

Figure 4.12: Differences between simulated $N^{60}(P_i)$ and filtered, by least squares collocation, $\tilde{N}^{60}(P_i)$ geoid undulations in the box $\varphi \in [-65°,-45°]$, $\lambda \in [40°W,20°E]$; units are meters. The differences range from +60 to -40 centimetres.

In Fig. 4.12 we show the differences $\tilde{N}^{60}(P_i)$ - $N^{60}(P_i)$ in our test area. We can observe something similar to a Gibbs effect with deterioration near the boundaries of the box.

It is clear that, for data in a limited area, this filter is not able to select adequately the frequencies up to k_0.

4.3 Summary of the results

The detailed analysis of the filtering procedures is necessary to take into account the different resolution of the geoid and the altimetric sea surface height. To get altimetric data and geoid spectrally consistent by filtering the altimetric data, it is necessary to find a common representation.

We studied two different approaches. The first (*global*) consists of the extension of the altimetric sea surface height as to cover all the Earth's surface and then in the representation of the data with the spherical harmonic functions. The second (*local*) consists of the study of the data considering a limited area like an ocean box. Here it is possible to use the 2D-Fourier representation and to apply a suitable low-pass filter.

The *local* approach has an accuracy of 3 cm. These results are obtained with the application of an anisotropic 2DButterworth low-pass filter on the data in the limited ocean box.

The results are better using the *global* approach. In order to be able to expand altimetric data into a series of spherical harmonics, all land areas (and ocean data gaps) have to be filled with data as well. We showed that the best results are obtained using a Jekeli-Wahr filter over a complete surface obtained with the "iterative procedure". In this case the accuracy of the filtering procedure is of 3 cm on all ocean surface and less than 1 mm over our ocean box.

5 The profile approach

5.1 Gridding – an undesirable filtering

Radar altimetry performs observations along profiles: The basic pulse repetition frequency for the range measurements is about 1KHz. Onboard software performs an averaging to 10Hz (TOPEX) or 20Hz (ESA missions) observations which are transmitted to the ground segment, where a further post-processing generates one second mean values for the altimeter range. The 1Hz range values are usually taken for any follow-on processing.

According to their mean ground velocity altimeter satellites provide every 6.5 – 7 km a one second mean value of the range measurements. This along-track resolution is in contrast to the rather large spacing of neighbouring ground tracks. For TOPEX the equatorial distance of neighbouring ground tracks is more than 300 km; ESAs altimetry missions (ERS-2 and ENVISAT) have a ground track spacing of about 80 km. In both cases there are large unobserved diamond shaped areas in between the profiles.

Gridding is a process to estimate from irregular distributed data parameter values on the nodes of a regular equally spaced grid. For satellite altimetry this gridding is of particular difficulty: first, the interpolated values at grid nodes in the centre of any non-observed diamond shaped area will be a mean of all measurements available on the surrounding profiles. Second, the surrounding profiles are observed at different times such that the interpolated value is also a temporal mean. Thus gridded data is already smoothed in space and time and the degree of smoothing depends on the distance to the observed profiles and on the actual observation times of the surrounding profiles (in general, the latter is not at all taken into account).

To circumvent this spatio-temporal fuzziness an approach has been developed to avoid any initial gridding, to stay as long as possible on the profiles and to perform necessary computations with the high resolution profile data. The procedure is further on called "profile approach".

5.2 Striping pattern of GRACE – filtering required

GRACE gravity fields realize essential improvements over previous estimates of the Earth gravity field and justify to recover the dynamic ocean topography (DOT) by subtracting geoid heights N from sea surface heights h, recall the basic equation

$$\zeta = h - N \tag{1}$$

However, even the latest GRACE satellite-only gravity fields (e.g. ITG03S) exhibit a meridional striping, an artifact of GRACE processing which does not represent geophysical signals. This is illustrated in Figure 5.1, top panel.

The cause of these striping pattern is not yet completely understood. There are some high frequent mass movements in the Earth system, like ocean tides or the variations in the Earth atmosphere. Their gravitational effect has to be reduced from the precise GRACE observations. However, for a fixed point on Earth GRACE samples these processes only very seldom, such that severe alias effects arise: The high frequent signal appears only with a rather long

alias period. For some of these effect the alias period is much longer than the period used for estimating gravity fields (typically a month). Any error in the modelling of the high frequency signal will consequently cause a (more or less) constant error in the gravity field.

Another cause for the striping pattern may be the sensitivity of the GRACE K-band range rate observation, taken between the twin satellites. This type of observation provides extremely precise along-track information but has no sensitivity across-track. Finally, due to the decaying orbit there is also a changing ground track pattern.
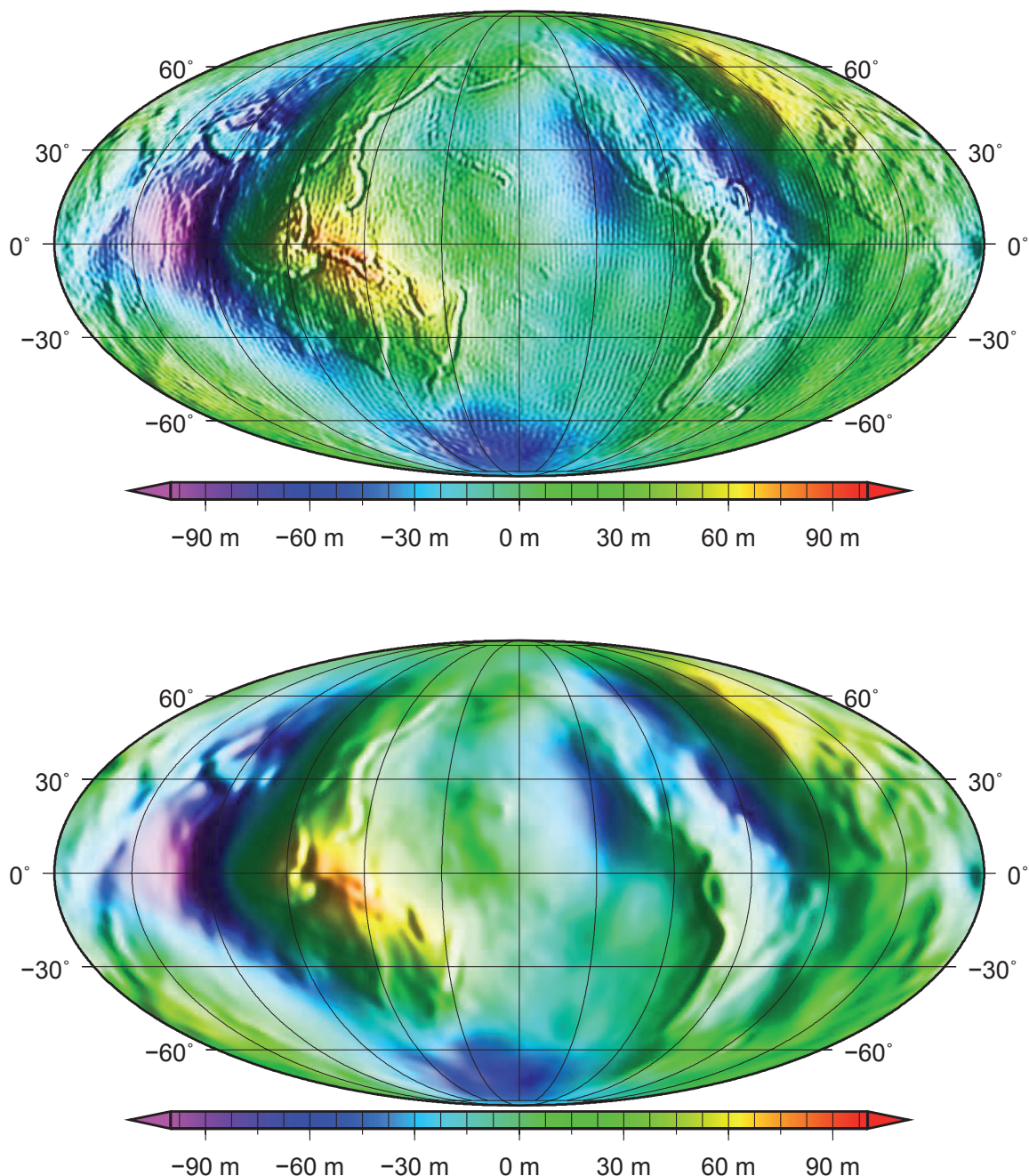

Figure 5.1 Geoid of ITG03S, one of the latest GRACE-only gravity field models. The top panel highlights the striping pattern by showing the geoid as an artificially relief, illuminated from the left. The bottom panel show the geoid after filtering the spectrum by a Gauss-type filter with 200 km filter radius.

Anyway, in order to remove the artificial striping a smoothing has to be applied. The investigations described in the previous section 4 have shown that the Gauss-type filter seems to provide the most reasonable results. Therefore the Gauss-type filter of Jekeli-Wahr (JW) has been applied to remove the artifical striping (see Equation (4.6) and (4.7) of section 4.1.1). As the gravity field models are provided by spherical harmonics (SH) the JW-filter can be applied in the spectral domain. In order to keep as much geoid signal as possible, but to filter strong enough to remove the striping pattern, a filter radius of $\alpha_r = 200$ km (according to Equation (4.7) this correspond to degree $k_0 = 72$) was found to be the most appropriate choice. The result of the filtering is shown in Figure 5.1, bottom panel.

5.3 Discrepancies between 2D- and 1D-filtering

This filter operation, indicated by the notation $2D_{JW}[\bullet]$ should be consistently applied to both quantities of Eqn 1, the sea surface heights h and the Geoid undulations N

$$\zeta = h - N = 2D_{JW}[h - N] = 2D_{JW}[h] - 2D_{JW}[N] \qquad (5.1)$$

The altimeter profiles, however, are only available in the spatial domain. A spectral representation of the sea surface heights is not available and difficult to construct as sea surface heights are not defined over land. Thus the equivalent spatial representation of the JW filter should be applied to the altimeter profiles in order to consistently filter both quantities, geoid and sea surface. The JW-filter is an isotropic, two-dimensional filter and can be applied to data distributed only along the profiles. Thereby the two dimensional filter $2D_{JW}[\bullet]$ reduces itself to a one dimensional filter, indicated in thefollowing by $1D_{JW}[\bullet]$ (c.f. Figure 5.2).
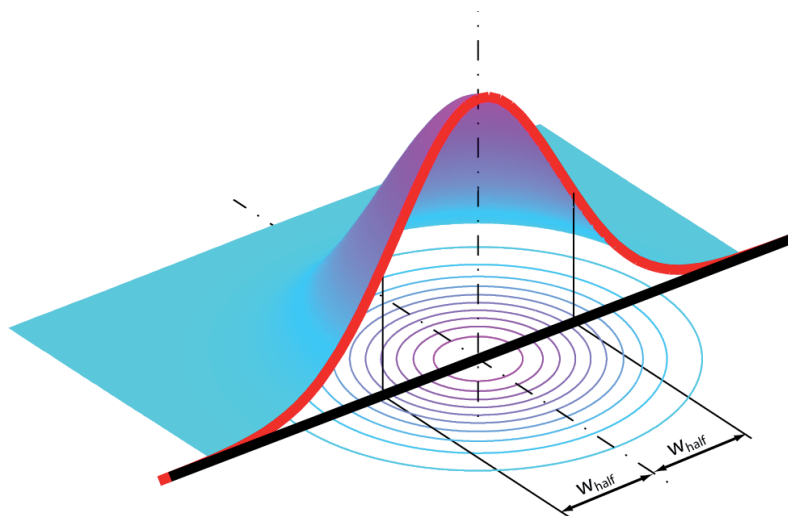

Fig. 5.2 The shape of the two dimensional Gauss-type filter (blue surface) and the effective filter if applied to one-dimensional profile data.

However, the 1D filtering of the altimetry profiles is not equivalent to a 2D filtering of laminar distributed data. Considering e.g. any mean sea surface in a neighbourhood of a trench, then the 2D filtering along a profile following this trench will raise the filtered sea surface heights due to the higher sea surface sidewards of the trench while the 1D filtering along the profile preserves the low sea surface heights along the grounding line of the trench. Figure 5.3 illustrates these conditions in detail.
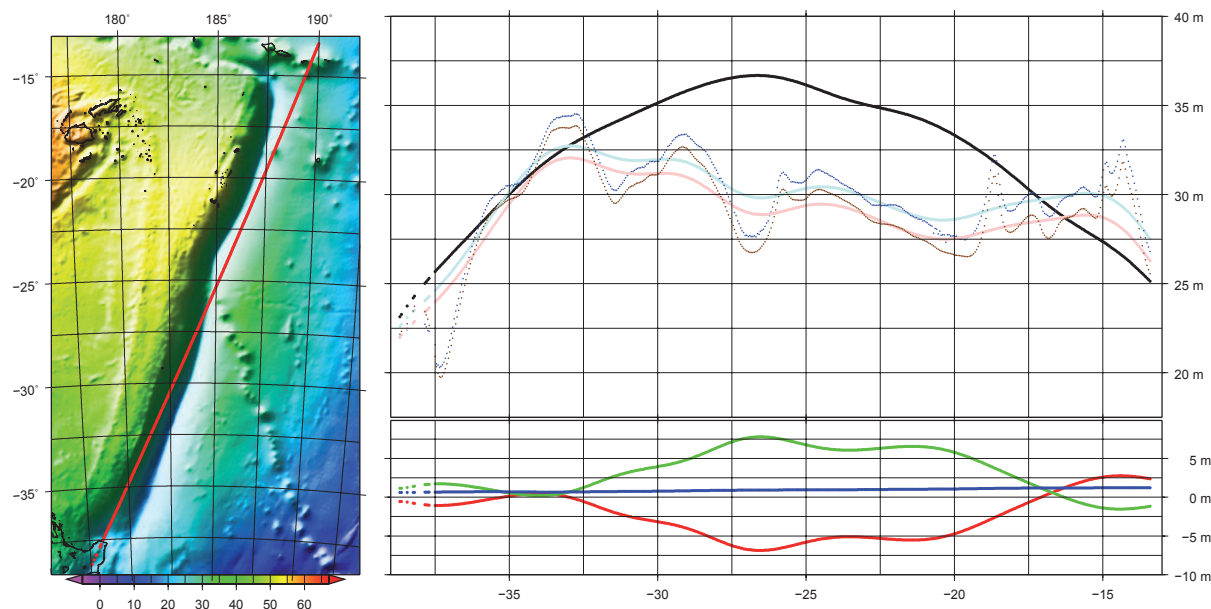

Fig. 5.3 Case study for the impact of 1D filtering of sea surface height profiles neighbouring a trench area. The left panel shows an ascending TOPEX-EM track close to the Kermadec and Tonga trenches North-East of New Zealand. The upper right panel shows the observed sea surface height profile (h$_i$(Jason1), blue dotted line), the 1D filtered sea surface height profile (1D(hi), light blue solid line), and the geoid undulation 2D$_{JW}$(N$_{SH}$) (black solid line) computed from the spectrally smoothed GRACE-only model ITG03S. The lower right panel shows in red the differences 1D(h$_i$) - 2D$_{JW}$(N$_{SH}$), in green the filter correction, and in blue the final estimate of the DOT profile.

5.4 The filter correction

In order to compensate these systematic differences between a 2D filtering of laminar data and the 1D filtering of profile data a filter correction has been developed in the following way: The identity

$$2D_{JW}[h] = 1D_{JW}[h] + (2D_{JW}[h] - 1D_{JW}[h]) \tag{5.2}$$

provides a relationship between 2D- and 1D-filtering and at the same time identifies the right hand term in round brackets as the necessary correction. This correction term can be approximated by a filter operations applied to a global continuous surface with a similar spatial resolution as the sea surface. A high resolution geoid, represented by a spherical harmonic series N_{SH}, is such a proxy for the sea surface. It is first sampled along the altimeter profiles at those points N_i where altimeter measurements are available. Then, the geoid is filtered twice: once along the profiles using the 1D spatial representation of the JW filter, giving $1D_{JW}[N_i]$ and second by applying the same JW filter on the spherical harmonic representation N_{SH} of the geoid, giving $2D_{JW}[N_{SH}]$. If the last quantity is evaluated at those points where altimeter

measurements are available, notated as $2D_{JW}[N_{SH}]_i$ then the difference

$$2D_{JW}[N_{SH}]i \ - \ 1D_{JW}[N_i] \tag{5.3}$$

defines the desired *filter correction*. Inserting Eqn (5.3) into Eqn (5.2) gives

$$2D_{JW}[h] \approx 1D_{JW}[h] + (2D_{JW}[N_{SH}]i \ - \ 1D_{JW}[N_i]), \tag{5.4}$$

a recipe to approximate the desired 2D-filtering of sea surface heights by a 1D-filtering performed along the profiles.

Initially, the EIGEN-GL04c (a hybrid model, developed up to degree/order 360 by combining GRACE and Laser observations with high resolution surface gravity data) was used to derive the filter correction. With EGM08 [Pavlis et al. 2008] an ultra high resolution gravity field, developed up to degree and order 2160, became available. Formally, EGM08 resolves spatial structures of 5' extension which corresponds to 9 km on the Earth surface. Thus the spatial resolution of EGM08 is rather consistent with the along-track resolution provided by the 1Hz altimeter data. Therefore the latest version of the filter correction is based on EGM08. Figure 5.4 shows the global pattern of the filter correction, computed for the ground tracks of a common cycle of Jason1 and TOPEX-EM (shifted ground tracks).
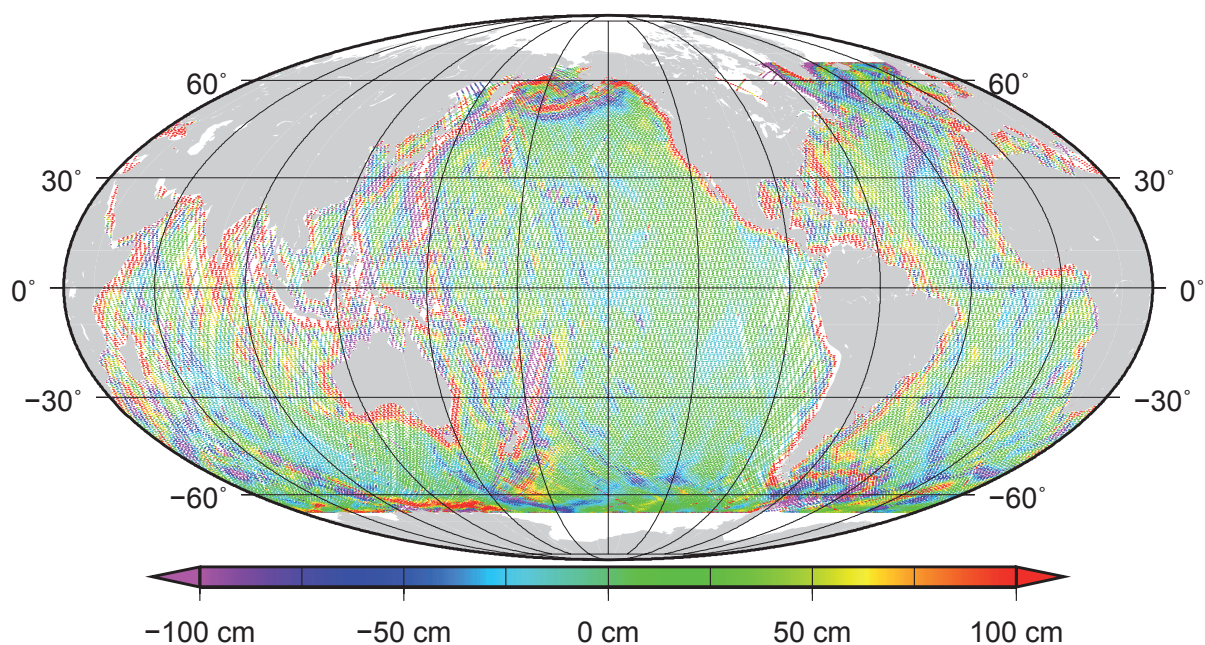

Fig. 5.4 The filter correction compensating the systematic differences between 1D filtering along profiles and 2D filtering in the spectral domain. The correction was derived with the ultra-high resolution gravity field EGM08 and is shown for the common 10-day ground track pattern of Jason-1 and TOPEX-EM (with shifted ground tracks)

5.5 The final approach

The filter correction, Eqn. (5.3) and the recipe, Eqn (5.4), developed above can now be applied to Eqn (5.1) such that

$$\zeta = 1D_{JW}[h] - 2D_{JW}[N] + (2D_{JW}[N_{SH}]i - 1D_{JW}[N_i]) \qquad (5.5)$$

completes the final strategy to estimate the DOT along altimeter profiles and to apply consistent filter oprations on both, sea surface heights and the geoid undulations.

The approach consist in following steps

1. decide on a filter radius α_r keeping as much geoid information as possible, but large enough to remove the undesirable striping pattern

2. compute a filter correction according to Eqn (5.3) using a high resolution geoid as a global surface providing at the same a proxy for the high resolution sea surface

3. apply the 2D-filter on the spectrum of a satellite-only gravity field, compute and sample the geoid at altimeter measurement points

4. apply the 1D-filter on the sea surface heights along the altimter profiles

5. Compose everything according to Equation (5.5)

Figure 5.5 provides a "snapshot" of the DOT estimated with the altimeter profiles acquired during a 10-day period.approach. A yearly mean DOT, estimated by the profile approach is shown in section 6.1 below.
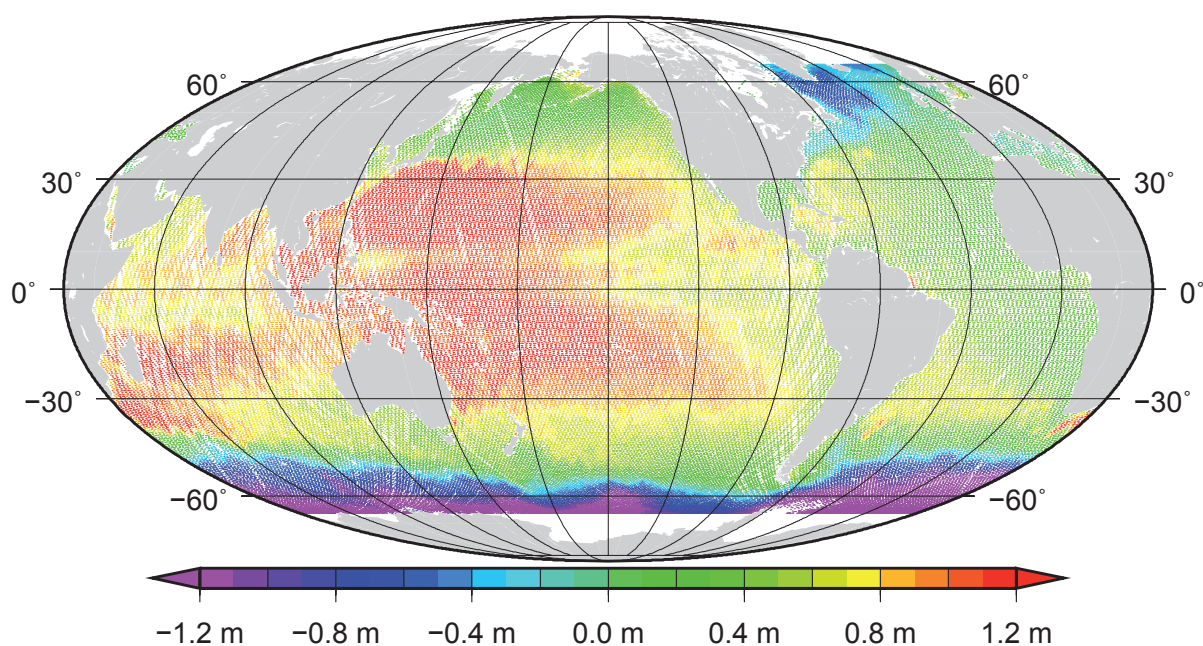
Fig. 5.5 Snapshot of DOT for a common 10-day cycle of TOPEX-EM and Jason-1, estimated with the "profile approach". It is remarkable that already data from a 10-day period is able to recover the large scale pattern of the DOT that are to be expected from oceanographic results

6 Examples of DOT

In this section different DOT estimates are shown and compared with each other. Section 6.1 gives two examples of DOT estimates, resulting from this study. Section 6.2 shows external estimates of the DOT and section 6.3 performs some comparisons
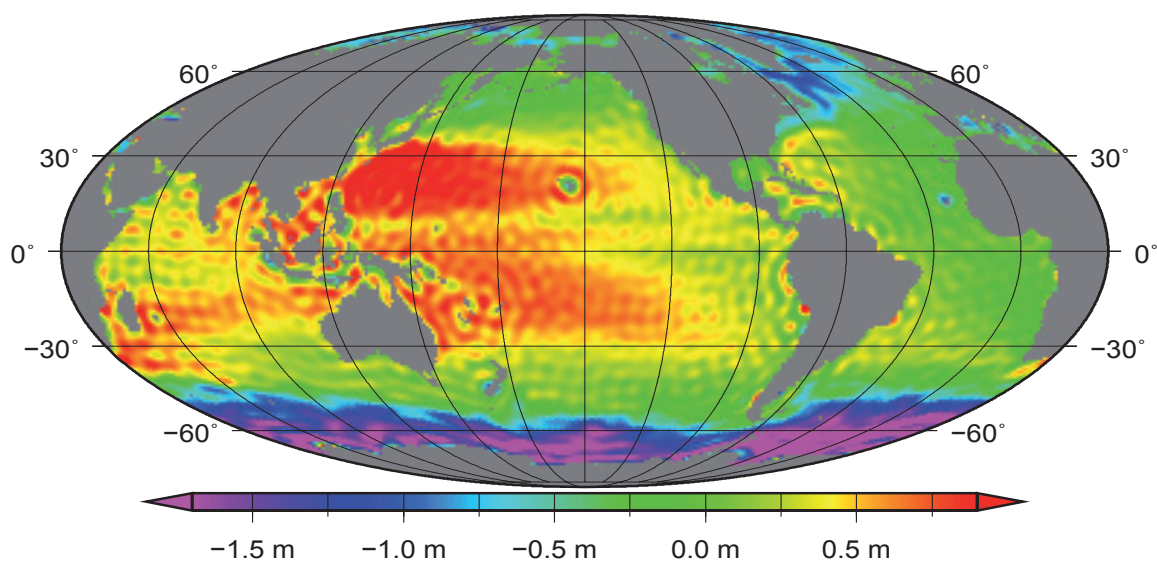
6.1 DOT estimates of this study

Fig. 6.1 DOT estimate derived with the "global approach" described in section 4.1 Land areas are filled using the iterative procedure described in 4.1 and the mean sea surface CLS01 are considered on the oceans. A cut-off filter up to degree 60 is applied to the spherical harmonics coefficients derived from the "complete" surface.
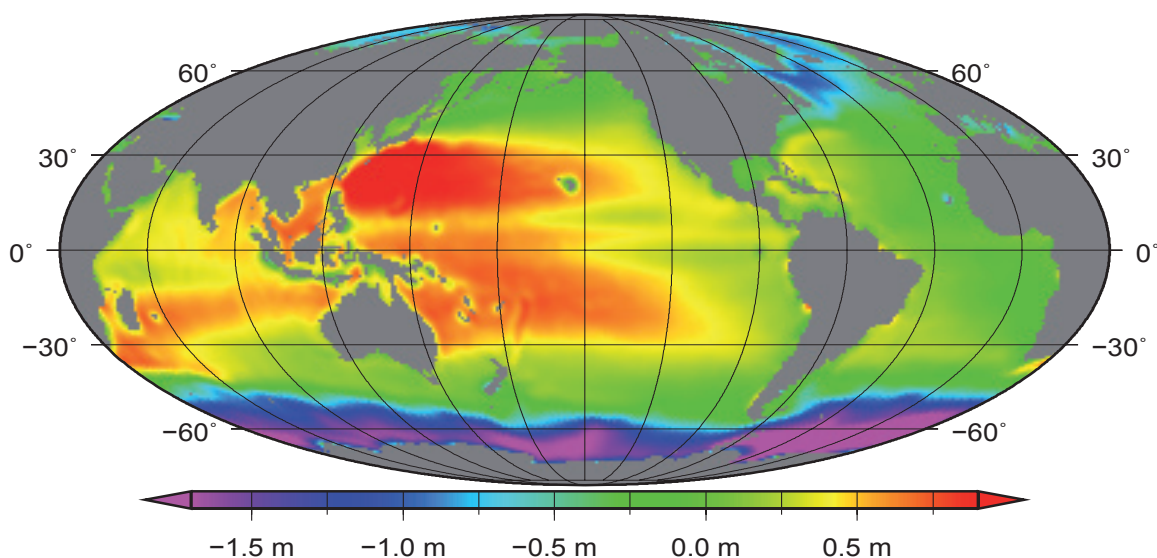

Fig. 6.2 DOT estimate derived with the "global approach" described in section 4.1 Land areas are filled using the iterative procedure described in 4.1 and the mean sea surface CLS01 are considered on the oceans. A Gauss filter with radius of 250 km is applied to the spherical harmonics coefficients derived from the "complete" surface.
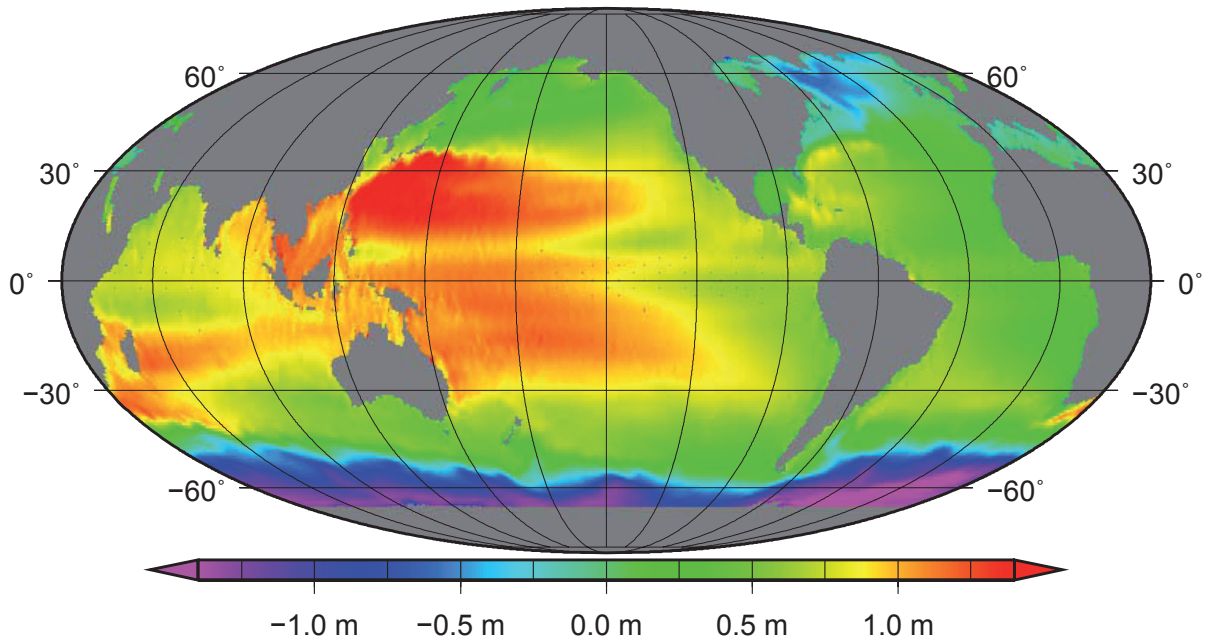
Fig. 6.3 Mean DOT for year 2004, derived with the "profile approach" described in section 5. Data from the ground tracks of Jason1 and TOPEX-EM (shifted ground tracks) has been used.

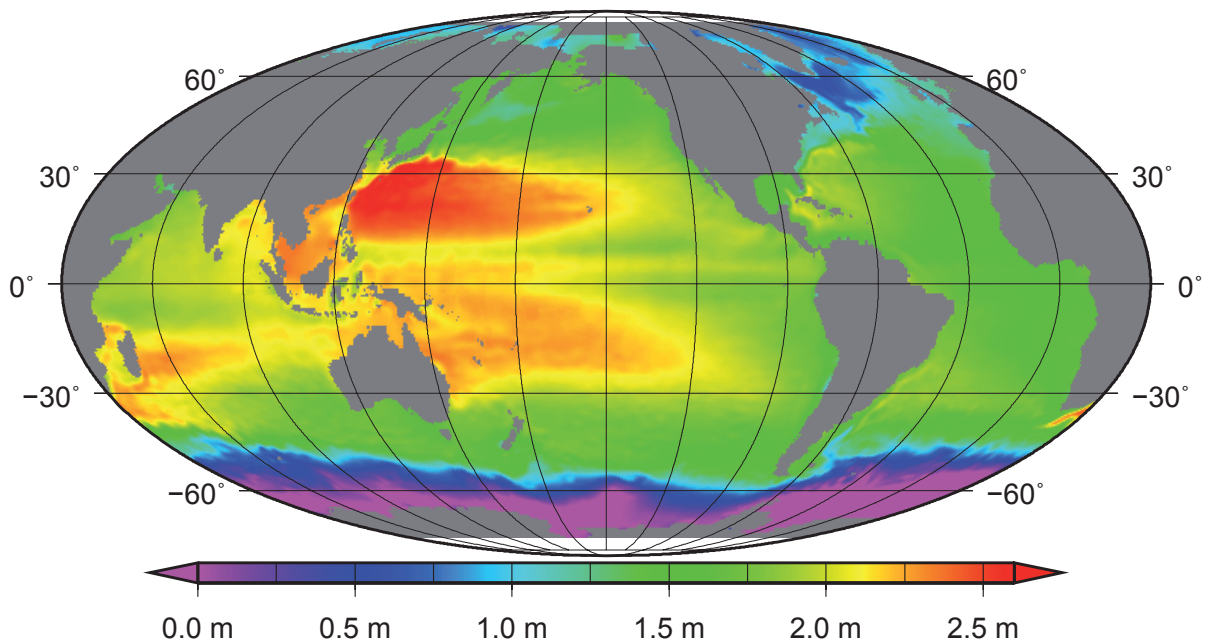## 6.2 Non-geodetic estimates of the DOT

Fig 6.4 DOT of Rio [2005]. Rio05 is computed over the 1993-1999 period, with a multi-variate analysis using hydrographic data, surface drifter velocities and altimetry. The guess used is based on both the CLS01 MSS - EIGEN-GRACE 03S geoid and the Levitus ,98 climatology (referenced to 1500 dbar). Note, the colour scale is not centered to zero in order to make the DOT pattern comparable to the plots of the geodetic estimates (Fig. 6.1 and 6.2).
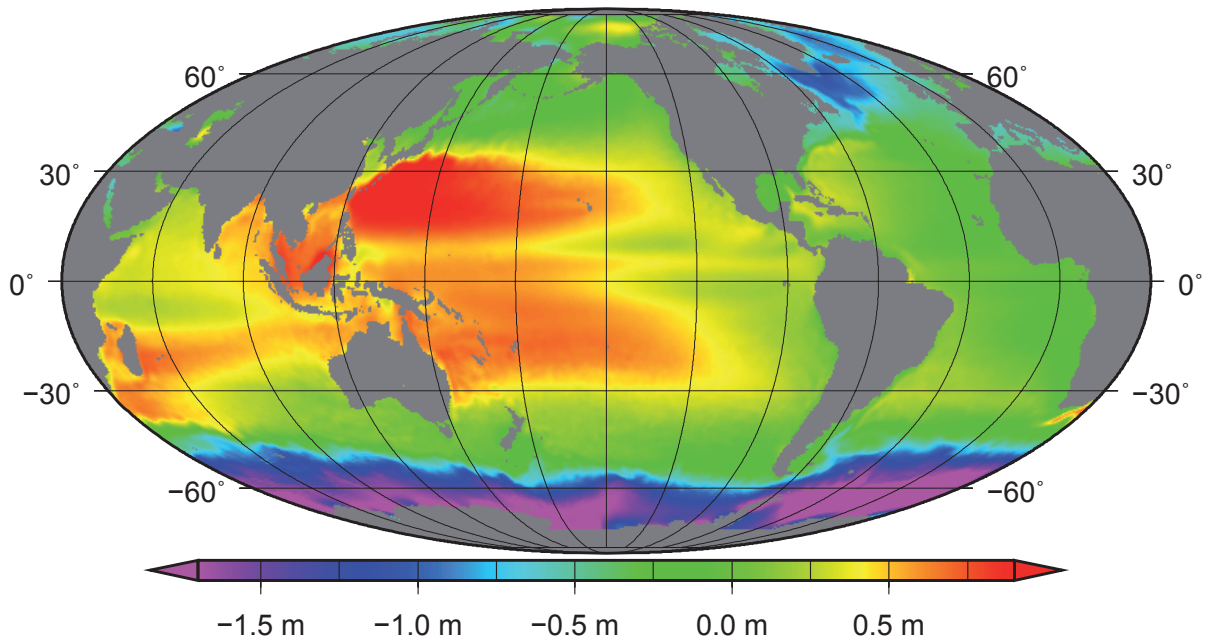
Fig. 6.5 DOT of Maximenko & Niiler. Note, the colour scale is not centered to zero in order to make the DOT pattern comparable to the geodetic estimates (Fig. 6.1, 6.2, and 6.3)
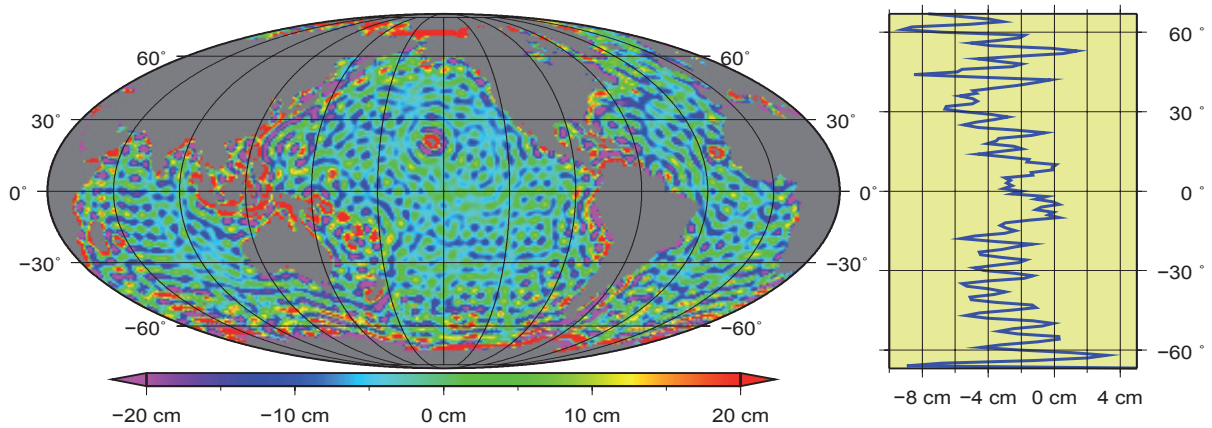
6.3 Comparisons

Fig. 6.6 Differences between the DOT shown in Fig. 6.1 and the DOT estimate of Maximenko & Niiler (Fig. 6.5). The lateral mean of the differences is shown in the panels on the right.
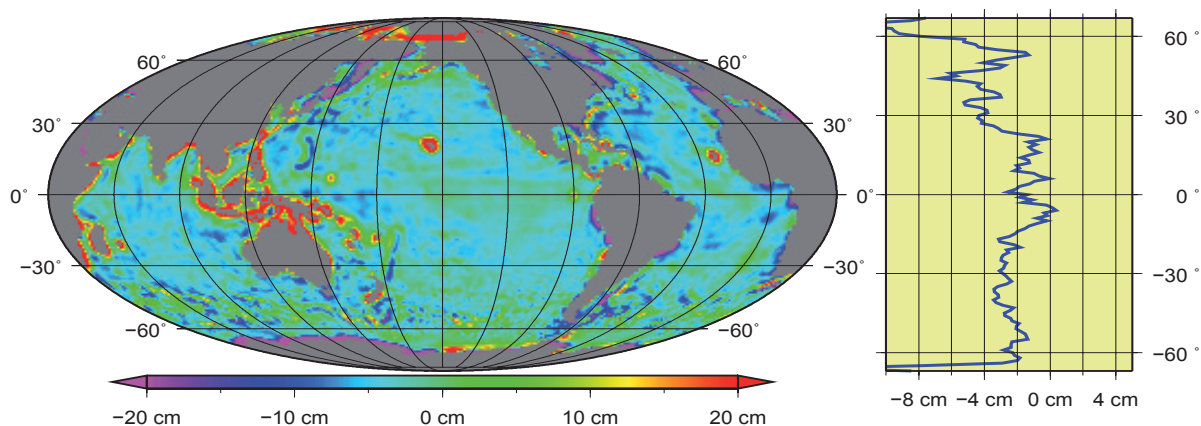
Fig. 6.7 Differences between the DOT shown in Fig. 6.2 and the DOT estimate of Maximenko & Niiler (Fig. 6.5). The lateral mean of the differences is shown in the right panel.
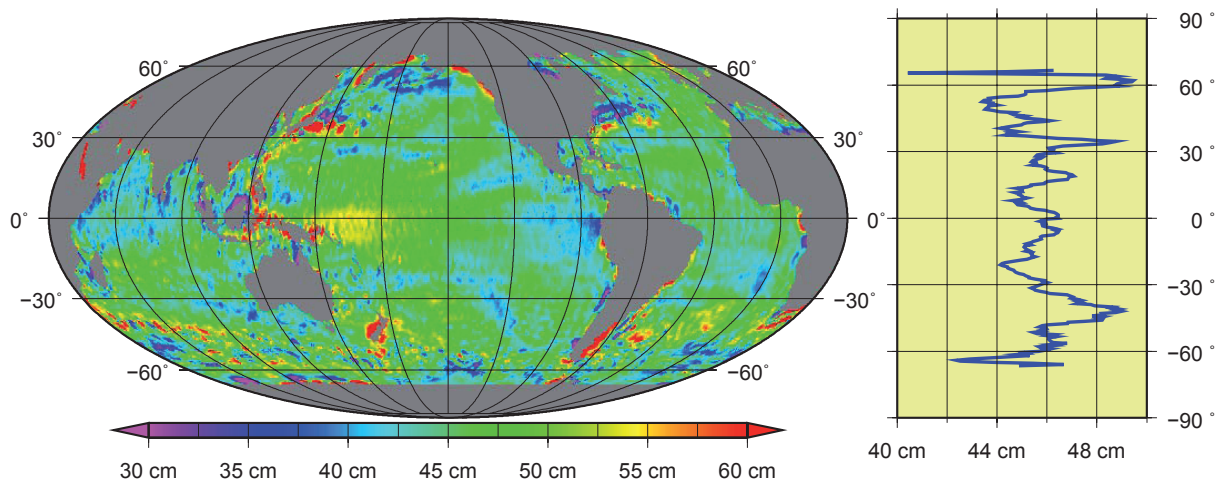

Fig. 6.8 Differences between the 2004 DOT shown in Fig. 6.3 and the DOT estimate of Maximenko & Niiler (Fig. 6.5). The lateral mean of the differences is shown in the right panel. Note, there is an offset of about +46 cm. Note also, the geodetic DOT is a mean for the year 2004 only while the averaging periods of the Maximenko & Niiler DOT is 1993-1999.
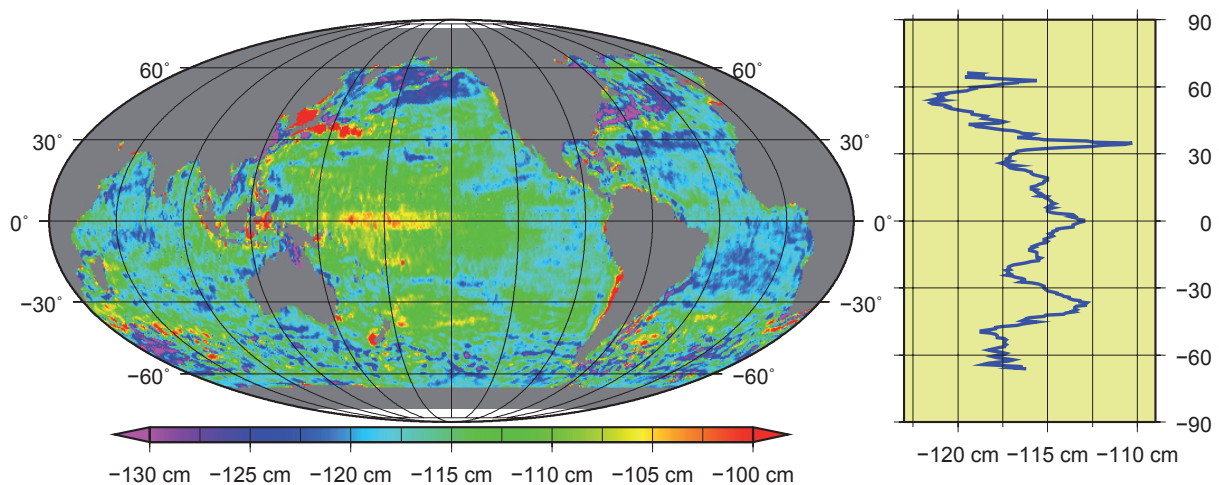

Fig. 6.9 Differences between the 2004 DOT shown in Fig. 6.3 and the DOT estimate of Rio (Fig. 6.4) . The lateral mean of the differences is shown in the right panel. Note, there is an offsets of about -115 cm. Note also, that the geodetic DOT is a mean for the year 2004 only while the averaging periods of Rio05 is 1993-1999.

7 Error propagation

7.1 Geoid errors

The recent models of the geopotential gravity field are available together with the complete statistical information. If the complete variance-covariance matrix is given, it is possible to derive not only the accuracy of each spherical harmonic coefficient (main diagonal of the matrix) but also all the correlations existing between the coefficients of the model.

In case of linear dependency, the law of covariance propagation is simple. Given a variable x, with its variance-covariance matrix C_{xx} known, the variance-covariance matrix of the variable $y = Ax+b$ is given by

$$C_{yy} = AC_{xx}A^{T} \tag{7.1}$$

Our problem is to derive the full variance-covariance matrix C_{NN} of the geoid undulations in a given area, starting from the knowledge of the full variance-covariance matrix C_{TT} of a selected geopotential model. This is a linear problem and in matrix form it can be written as:

$$N = AT \tag{7.2}$$

Applying (7.1) we obtain:

$$C_{NN} = AC_{TT}A^{T} \tag{7.3}$$

To build the matrix A it is necessary to establish the explicit relation between the spherical harmonic coefficients Y_{lm} and the geoid undulations $N(\varphi_i, \lambda_j)$ in

the selected area ($\varphi_i \in [\varphi_{\min}, \varphi_{\max}]; \lambda_j \in [\lambda_{\min}, \lambda_{\max}]$):

$$N(\varphi_i, \lambda_j) = R \sum_{\ell=2}^{L} \sum_{m=-\ell}^{\ell} y_{\ell m} Y_{\ell m}(\varphi_i, \lambda_j) \tag{7.4}$$

The geopotential model is considered up to the maximum degree $L = 60$, that means 3717 coefficients are to be considered. The geoid undulations are computed in the selected ocean box = [-45°, -65°; 40°W, 20° E]. For a sampling equal to 1°, this corresponds to 1281 points.

Therefore the dimension of the matrix A is (1281 × 3717), the dimension of C_{NN} is (1281 × 1281) and of C_{TT} (3717 × 3717).

The matrix A is the matrix that, multiplied with the vector of the harmonic coefficients, gives us the geoid undulations in the selected area. Each row corresponds to a point of our box and each column corresponds to one of spherical harmonic coefficients. The definition of the matrix A is not unique, but depends on the order chosen of the spherical harmonic coefficients and of the point of the grid.

An example is:

$$
A^T = R \begin{bmatrix}
P_{00}(\varphi_1)\cos 0\lambda_1 & P_{00}(\varphi_1)\cos 0\lambda_2 & P_{00}(\varphi_1)\cos 0\lambda_3 & \cdots & P_{00}(\varphi_2)\cos 0\lambda_1 & P_{00}(\varphi_2)\cos 0\lambda_2 & \cdots & P_{00}(\varphi_I)\cos 0\lambda_J \\
P_{10}(\varphi_1)\cos 0\lambda_1 & P_{10}(\varphi_1)\cos 0\lambda_2 & P_{10}(\varphi_1)\cos 0\lambda_3 & \cdots & P_{10}(\varphi_2)\cos 0\lambda_1 & \cdots & \cdots & P_{10}(\varphi_I)\cos 0\lambda_J \\
P_{20}(\varphi_1)\cos 0\lambda_1 & P_{20}(\varphi_1)\cos 0\lambda_2 & P_{20}(\varphi_1)\cos 0\lambda_3 & \cdots & P_{20}(\varphi_2)\cos 0\lambda_1 & \cdots & \cdots & P_{20}(\varphi_I)\cos 0\lambda_J \\
\cdots & \cdots & \cdots & \cdots & & & & \cdots \\
P_{11}(\varphi_1)\cos 1\lambda_1 & P_{11}(\varphi_1)\cos 1\lambda_2 & \cdots & \cdots & & & & \cdots \\
P_{21}(\varphi_1)\cos 1\lambda_1 & P_{21}(\varphi_1)\cos 1\lambda_2 & \cdots & \cdots & & & & \cdots \\
\cdots & \cdots & \cdots & \cdots & & & & \cdots \\
P_{11}(\varphi_1)\sin 1\lambda_1 & P_{11}(\varphi_1)\sin 1\lambda_2 & \cdots & \cdots & & & & \cdots \\
P_{21}(\varphi_1)\sin 1\lambda_1 & P_{21}(\varphi_1)\sin 1\lambda_2 & \cdots & \cdots & & & & \cdots \\
\cdots & \cdots & \cdots & \cdots & & & & \cdots \\
P_{LL}(\varphi_1)\sin L\lambda_1 & P_{LL}(\varphi_1)\sin L\lambda_2 & \cdots & \cdots & \cdots & \cdots & \cdots & \cdots
\end{bmatrix}
\tag{7.5}
$$

We compute the full variance propagation considering three geopotential models:

- **CHAMP**: the model is derived from the data of the CHAMP mission, computed at the Technische Universität of München [Gerlach et al., 2003, Földváry et al., 2005]. For this model the full variance-covariance matrix up to the degree 60 is available.

- **GRACE**: the static gravity field model ITG-Grace03s is computed at the University of Bonn [Mayer-Gürr et al., 2006, Mayer-Gürr, 2006]. In this case the full variance-covariance matrix up to degree 180 is available.

- **GOCE**: the geopotential model computed in the HPF project, using simulated data of the next GOCE mission [Gruber et al., 2007]. In this case the full variance-covariance up degree 200 is available.

In our computation each model is considered only to the maximum degree 60 and each matrix is ordered following the order established by the matrix A, like in (7.5).

Fig. 7.1 shows the full variance-covariance matrices C_{TT}^{CHAMP}, C_{TT}^{GRACE}, and C_{TT}^{GOCE} of the CHAMP, GRACE and GOCE models, reduced up to the maximum degree 60 and order like in (7.5).

The main diagonal of each matrix contains the variances of all the coefficients. These variances can be reorganized obtaining the usual representation of the accuracy of the geopotential model. Fig. 7.2 shows the standard deviation of the coefficients of the CHAMP, GRACE and GOCE model, respectively.

Given the three matrices C_{TT}^{CHAMP}, C_{TT}^{GRACE}, C_{TT}^{GOCE} and the matrix A it is easy to perform the variance propagation to the geoid undulation in our ocean box applying eq. (7.3).

In this way we obtain the three matrices C_{NN}^{CHAMP}, C_{NN}^{GRACE}, C_{NN}^{GOCE} shown in Fig. 7.3. The k-th row (and the k-th column) of each matrix represents the correlation between the k-th point with all the others points of the grid. The diagonal of each matrix represents the variances of the points of the grid. The standard deviations of the geoid undulations resulting from the propagation are shown in Fig. 7.4.

In all three cases the accuracy is higher for low latitudes and we can observe that, as expected, the order of magnitude of the results is completely different. In this bandwidth (from 2 to 60) the GRACE model gives the best solution ($\sim 2\cdot10^{-4}$ m), then there is the GOCE solution ($\sim 2\cdot10^{-3}$ m) and finally the CHAMP solution (~ 10 cm).

From the same matrices we can also compute the correlations between each point of the box and all the other points. The correlation between the central point of the grid $P = [-55°, -10°]$ and all the other points are shown in the Fig. 7.5.

The three considered models show completely different patterns.

In the case of the CHAMP solution, the correlations have a clear central symmetry, which is probably related to the method used for the computation of the geopotential model: the energy integral approach.

In the case of the GRACE solution there is a longitudinal symmetry, which is related to the design of the GRACE mission: two satellites following each other and flying in an almost polar orbit.

Finally, in the case of the GOCE solution it is possible to observe a strong anti-correlation in latitude direction and a moderate correlation in longitude direction. This particular shape of the correlation is probably related again to the geometry of the problem (gradiometer instead of accelerometers) and to the particular solution adopted for the computation of the geopotential model.

The behaviour of the correlations remains the same also when other points of the grid are considered, instead of the central point.
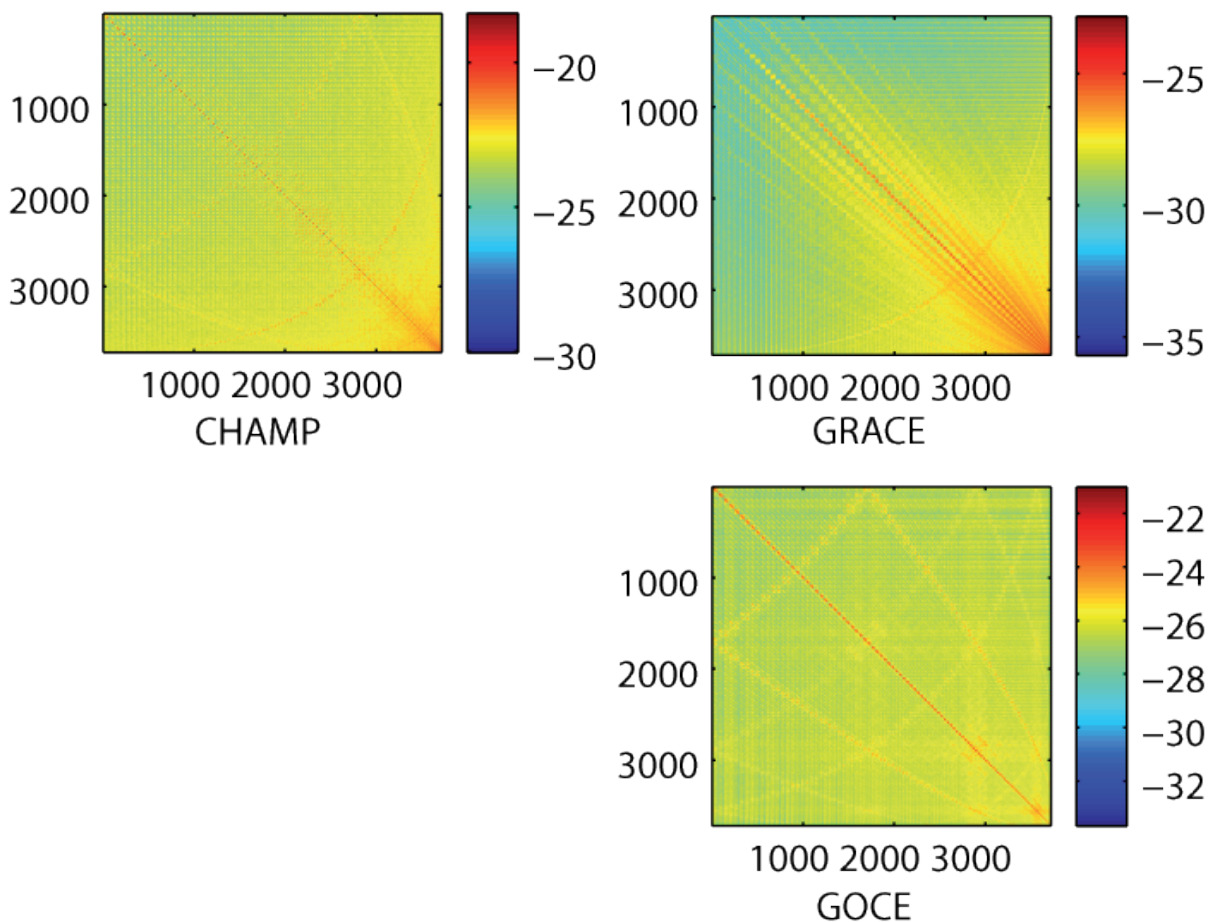

Figure 7.1 Full variance-covariance matrix of the geopotential model derived from CHAMP (top left), GRACE (top right) and GOCE (bottom) data. The harmonic coefficients are ordered by order, within each order they are sorted by degree with cosine and sine coefficients alternating.
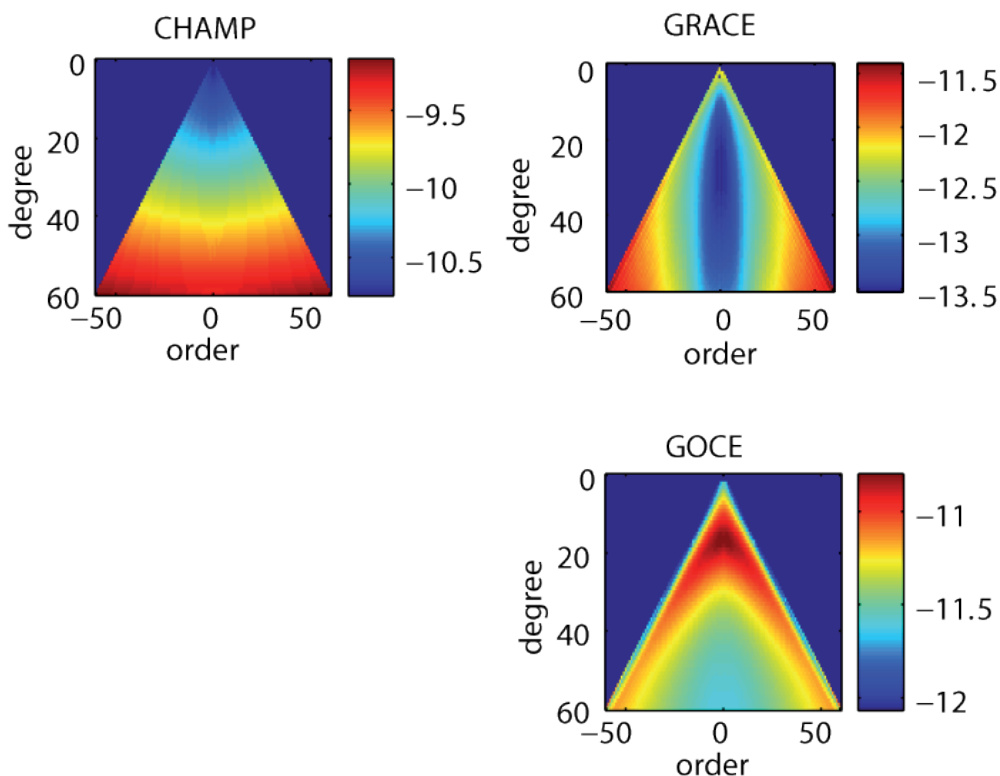
Figure 7.2 Standard deviation of the spherical harmonic coefficients of the geopotential model derived from CHAMP (top left), GRACE (top right) and GOCE (bottom)(direct solution) data. For the GRACE data we can observe a degradation towards the sectorial terms.
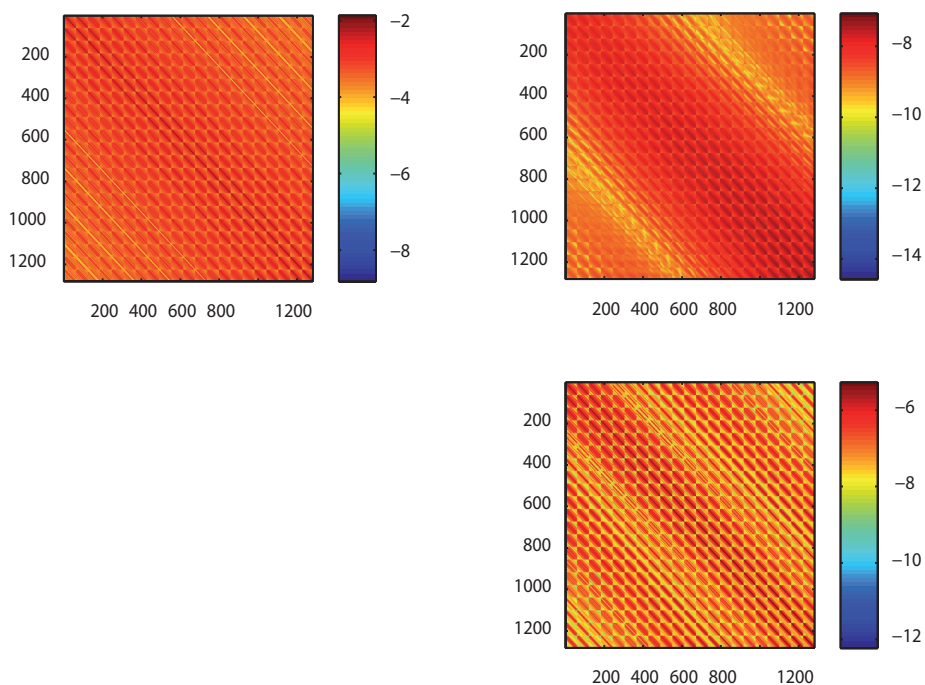

Figure 7.3 Full variance-covariance matrix of the geoid undulations in the ocean box = [-45°, -65°; 40°W, 20° E], obtained from the CHAMP (top left), GRACE (top right) and GOCE (bottom) models. The absolute values of the elements of the matrix ([m²]) are represented in logarithmic scale.
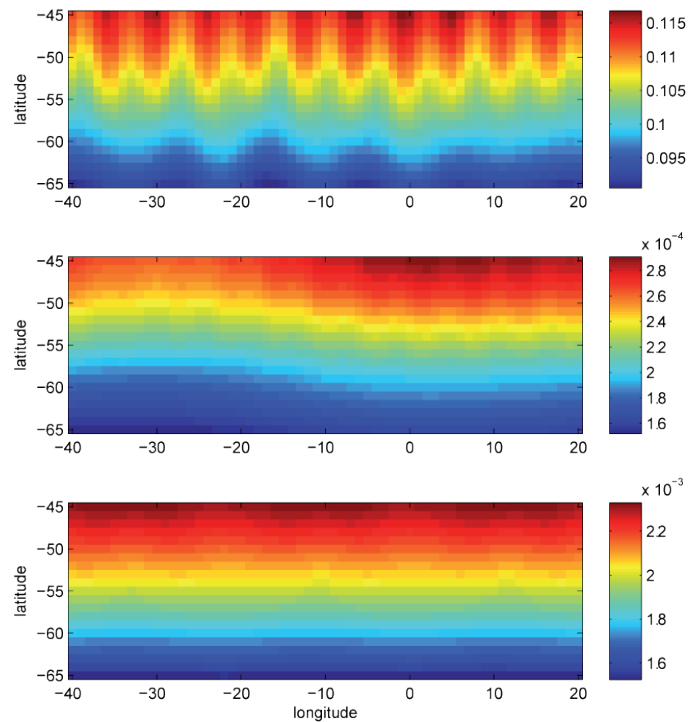
Figure 7.4 Standard deviations of the geoid undulations in the ocean box = [-45°, -65°; 40°W, 20° E], obtained from the CHAMP, GRACE and GOCE models (respectively from top to bottom). The units are metres.

Figure 7.5 Correlations between the central point, P=[-55°, -10°] of the selected box, and the other points of the grid, obtained from the CHAMP, GRACE and GOCE models (respectively from top to bottom). The units are meter x meter.

The knowledge of the full stochastic model of the geoid undulation, together with the variance-covariance information on the sea surface height, represents the complete statistical information of the absolute sea surface topography. In this way we can apply rigorous error propagation without approximations.
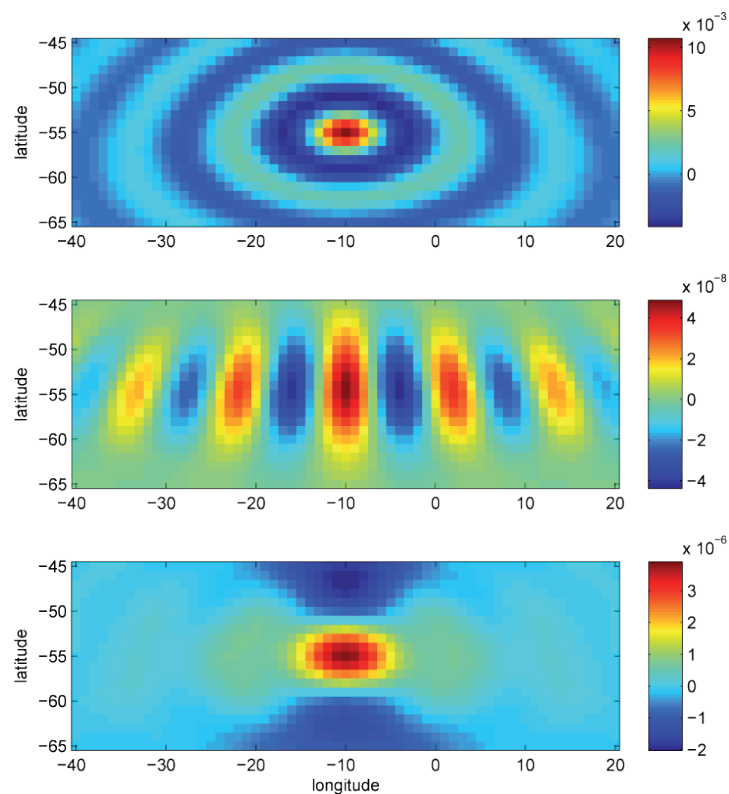
A further step will be the assimilation of the geodetic SST into an ocean model. The stochastic model of the ocean model will be combined with altimetry and geoid errors. Also in this case it is important to have a complete statistical knowledge of the data involved.

7.2 Autocovariance function for altimetry

For the sea surface heights a reliable error estimate is required as well. However, sea surface heights are not a result of a least squares estimation and therefore there is no corresponding variance-covariance matrix available. Instead sea surface heights are basically obtained by subtracting the altimeter range measurement, corrected for a considerable number of geophysical and environmental effects, from the satellite height which in turn has been determined by a dynamic, reduced dynamic or a kinematic orbit determination process. Consequently the error budget of the sea surface heights depends on many components, the precision of the range measurement, the accuracy of the models taken to correct the altimeter range, and the error of the radial component of the orbit. It is difficult to get a realistic overall error budget.

Altimetry itself provides a powerful tool that allows to estimate the overall accuracy of sea surface heights: The ground tracks, composed of ascending and descending passes, result in crossings, such that the sea surface height at those crossovers can be derived twice. This redundancy can be used to estimate the radial component of the altimetric errors. The difference between the two realizations of sea surface heights, called crossover differences, should vanish under the assumption, that there are no errors and no variations in sea level. In fact, even the crossover differences derived from measurements very close in time (thereby excluding any sea level variation), do *not* vanish and can be used to estimate by least squares the parameters of a model describing the radial error component. This process is called *crossover analysis*. Without describing more details it should be emphasized that the error estimate is a good indication of the overall error budget, as all error components are projected to the crossover differences.

In the context of this study, a rather ambitious crossover analysis has been performed. A discrete crossover analysis [Bosch, 2007] is used for the common estimation of relative range biases and radial errors of all contemporaneous altimeter systems. The cross-calibration is performed globally for up to five altimeter satellites operating simultaneously (TOPEX, ERS-1, ERS-2, Jason1, ENVISAT, and GFO). The total set of single- and dual-satellite crossover differences, performed in all combinations and with a maximum time difference of three days, creates a strong network with high redundancy. It enables a reliable and dense sampling of the radial errors of all satellites. Details of this multi-mission crossover analysis are described in Bosch [2005] and Bosch and Savcenko [2007]. As a result of this analysis complete time series of radial errors of all satellites are obtained for the whole mission lifetime. It is then straightforward to estimate an empirical auto-covariance function for every satellite. This is shown in Figure 7.6
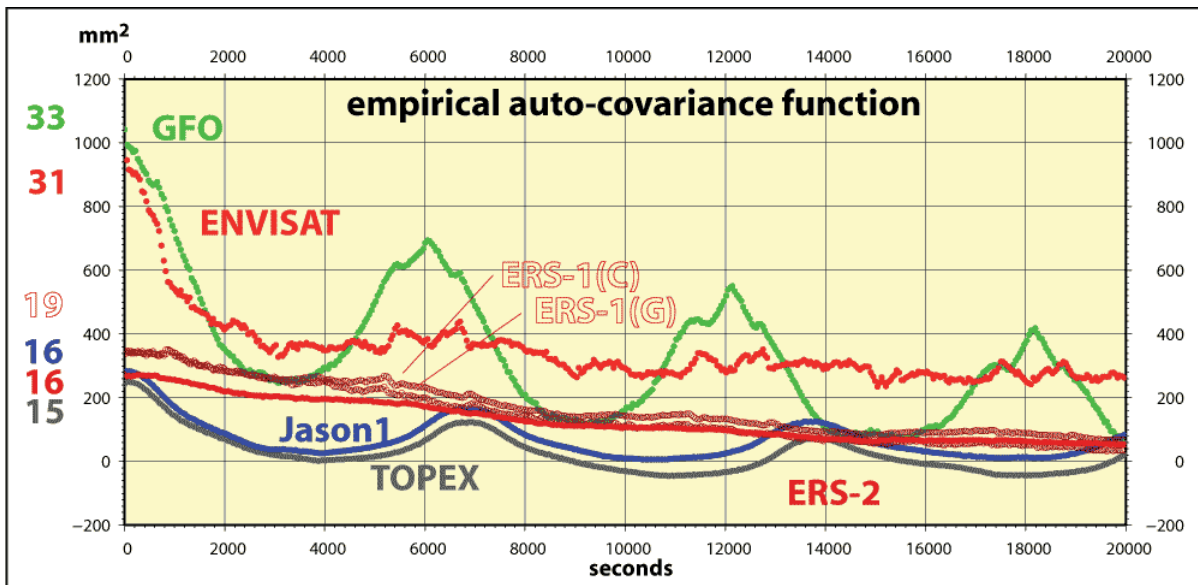
Fig 7.6 Empirical auto-covariance function for altimeter missions cross-calibrated by a multi-mission crossover analysis. The figures on left give the square root of the variances.

From Figure 7.6 it is clearly visible that the altimeter systems have different accuracy. TOPEX, Jason1, and ERS-2 perform best and have a radial error of 15 and 16 mm respectively. The accuracy of ENVISAT and GFO is degraded. For ENVISAT this is due to the so-called S-band anomaly which is not properly flagged in the mission data (meanwhile the S-band anomaly has been correctly edited). GFO suffers from the spare laser tracking and a poor orbit quality as the orbits are not yet based on one of the new GRACE gravity field models. The fact that the auto-covariance function increases again after approximately one revolution, is a clear indication that the radial error is still plagued by systematic, so called geographically correlated errors.

The empirical auto-covariance function is considered as the most reliable error characterization of the altimeter data. Any follow on-process (gridding or direct assimilation into a numerical model) has to use this function for a rigorous error propagation.

References

Albertella A. and R. Rummel, 2008: On the Spectral consistency of the Altimetric Ocean and geoid Surface. A One-dimensional Example, submitted to the Journal of Geodesy.

Bosch W. (2005): Simultaneous crossover adjustment for contemporary altimeter missions. ESAESTEC, SP 572, ESA/ESTEC

Bosch, W. (2007) Discrete crossover analysis (DCA). IAG Symposia, Vol. 130, 131-136, Springer, Berlin

Bosch, W. and R. Savchenko (2007): Satellite Altimetry: Multi Mission Cross Calibration. IAG Symposia, Vol. 130, 51-56, Springer, Berlin

Bosch W., R. Savcenko, F. Flechtner, C. Dahle, T. Mayer-Gürr, D. Stammer , E. Taguchi, and K.-H. Ilk (2008): Residual ocean tide signals from satellite altimetry, GRACE gravity fields, and hydrodynamic modelling. Submitted to Geophys. Research Letters, paper 2008GL036038

Brajovic J., 2005: Validierung von Schwerefeldmodellen mit terrestrischen Daten, Diplomarbeit, Technische Universität München, Institut für Astronomische und Physikalische Geodäsie.

Brigham E. Oran, 1974: The Fast Fourier Transform, Prentice-Hall, Inc., Englewood Cliffs, New Jersey.

Carrère, L., and F. Lyard (2003), Modeling the barotropic response of the global ocean to atmospheric wind and pressure forcing – comparisons with observations, Geophys. Res. Let., 30(6), 1275, doi: 10.1029/2002GL016473.Condi F. and C. Wunsch, 2004: Measuring gravity field variability, the geoid, ocean bottom pressure fluctuations, and their dynamical implications, Journal of Geophysical Research, 109, 10.1029/2002JC001727.

Daubechies I., 1992: Ten Lectures on Wavelets, SIAM, Philadelphia, Pa, USA.

Földváry L., D. Švehla, Ch. Gerlach, M. Wermuth, Th. Gruber, R. Rummel, M. Rothacher, B. Frommknecht, Th. Peters, P. Steigenberger, 2005: Gravity Model TUM-2Sp Based on the Energy Balance Approach and Kinematic CHAMP Orbits, Earth Observation with CHAMP, Results from Three Years in Orbit (eds.: Ch. Reigber, H. Lühr, P. Schwintzer, J. Wickert), S. 13-18, Springer, Berlin.

Ganachaud A., C. Wunsch, M.C. Kim and B. Tapley, 1997: Combination of TOPEX/POSEIDON data with a hydrographic inversion for determination of the oceanic general circulation and its relation to geoid accuracy, Geophysical Journal International, 128(3), 708-772.

Gerlach Ch., L. Foldváry, D. Švehla, Th. Gruber, M. Wermuth, N. Sneeuw, B. Frommknecht, H. Oberndorfer, TH. Peters, M. Rothacher, R. Rummel, P. Steigenberger, 2003: A CHAMP – Only Gravity Field Model From Kinematic Orbits Using the Energy Integral, Geophysical Research Letters, Vol. 30, No. 20, 2037.

Graps A., 1995: An Introduction to Wavelets, IEEE Comput. Sci. Eng. vol.2 n.2, 50--61.

Gruber T., 2000: Hochauflösende Schwerefeldbestimmung aus Kombination von terrestrischen Messungen und Satellitendaten über Kugelfunktionen, Scientific Technical Report STR00/16, GeoForschungsZentrum Potsdam.

Gruber T, R. Rummel and R. Koop, 2007: How to Use GOCE level 2 products, The 3rd International GOCE User Workshop, 6-8 November 2006, ESA/ESRIN Frascati Italy, SP 627.

Heiskanen W.A., H. Moritz, 1967, Physical Geodesy, W.H. Freeman and Company, San Francisco

Hernandez, F. and P. Schaeffer, 2000, Altimetric Mean Sea Surfaces and GravityAnomaly maps inter- comparisons AVI-NT-011-5242-CLS, 48 pp. CLS Ramonville St Agne.

Ilk, K.H., Flury, J., Rummel, R., Schwintzer, P., Bosch, W., Haas, C., Schröter, J., Stammer, D., Zahel, W., Miller, H., Dietrich, R., Huybrechts, P., Schmeling, H., Wolf, D., Riegger, J., Bardossy, A., Güntner, A., 2005: Mass Transport and Mass Distribution in the Earth System, Contribution of the New Generation of Satellite Gravity and Altimetry Missions to Geosciences, 2nd edition, GOCE Projectbüro TU München, GFZ Potsdam.

Jekeli C., 1981: Alternative methods to smooth the earth's gravity field, Rep. 327, d. Sci. & Surv., Ohio State University, Columbus.

Kaula W.M., 1966, Theory of Satellite Geodesy, Waltham, Mass.: Blaisdell Pub.Co.

Kaula, W.M. et al., 1970: The Terrestrial Environment: Solid Earth and Ocean Physics, NASA Contractor Report, CR-1579.

Le Grand, P., J-F. Minster, 1999: Impact of the GOCE gravity mission ocean circulation, Geoph. Res. Letters 26(13), 1881--1884.

Le Grand, P., 2001: Impact of the Gravity Field and Steady-State Ocean Circulation Explorer (GOCE) mission on ocean circulation estimates. Volume fluxes in a climatological inverse model of the Atlantic, J. Geophys. Res. (Oceans), 106, 19597--19610.

Le Provost, C., E. Dombrowsky, P. Le Grand, P.Y. Le Traon, M. Losch, F. Ponchaut, J. Schröter, B. Sloyan, N. Sneeuw, 1999: Impact of the GOCE mission for ocean circulation study, ESTEC 13175/98/NL/GD.

Losch M., B.M. Sloyan, J. Schröter and N. Sneeuw, 2002: Box inverse models, altimetry and the geoid: Problems with the omission error, Journal of Geophysical Research, 107, (C7) 10.1029/2001JC000855.

Losch M. and J. Schröter, 2004: Estimating the circulation from hydrography and satellite altimetry in the Southern Ocean: limitations imposed by the current geoid models, Deep-Sea Research I 51, 1131-1143.

Lyard, F., Lefevre, F., Letellier, T., and Francis, O. (2006), Modelling the global ocean tides: modern insights from FES2004. Ocean Dynamics, 56, 394–415, doi:10.1007/s10236-006-0086-x.

Mayer-Guerr, T., 2006: Gravitationsfeldbestimmung aus der Analyse kurzer Bahnbögen am Beispiel der Satellitenmissionen CHAMP und GRACE, Dissertation, University of Bonn

Mayer-Guerr, T., A. Eicker and K.-H. Ilk, 2007: ITG-Grace02s: A GRACE Gravity Field Derived from Short Arcs of the Satellites Orbit, Proceedings of the 1st International Symposium of the International Gravity Field Service „Gravity Field of the Earth", Istanbul.

Moritz H., 1980: Advanced Physical Geodesy, Wichmann, Karlsruhe.

Papoulis A. and M. S. Bertran, 1972: Digital Filtering and Prolate Functions, IEEE Transactions on Circuit Theory, vol. CT19, n.6, 674--681.

Pavlis N.K., S.A. Holmes, S.C. Kenyon and J.K. Factor, 2008: An Earth Gravitational Model to Degree 2160: EGM2008, presentation at EGU General Assembly 2008 Vienna, Austria, April 13-18, 2008

Reigber C., Schmidt R., Flechnter F., König R., Meyer U., Neumayr K., Schwintzer P., Zhu S, 2005: An Earth gravity field model complete to degree and order 150 from GRACE: EIGEN-GRACE02S. Journal of Geodynamics, 39(B1): 1-10.

Savcenko R. and W. Bosch (2007): Residual tide analysis in shallow water – contributions of ENVISAT and ERS altimetry. In: Huguette Lacoste (ed): ENVISAT Symposium 2007, ESA SP636, 2007

Savcenko R. and W. Bosch (2008): EOT08a - empirical ocean tide model from multi-mission altimetry. Report No. 81, Deutsches Geodätisches Forschungsinstitut (DGFI), München

Schröter J., M. Losch, B.M. Sloyan, 2002: Impact of the GOCE gravity mission on ocean circulation estimates: Part II. Volume and heat fluxes across hydrographic sections of unequally spaced stations, J. Geophys. Res. (Oceans), 107(C2).

Shum, C., N. Yu, and C. Morris (2001): Recent advances in ocean tidal science, J. of Geodetic Society of Japan, Vol. 47, No. 1, 528-537.

Slepian D., 1978: Prolate spheroidal wave functions, Fourier analysis and uncertainty. V. The discrete case, Bell. Syst. Tech. J., 57(5), 1371--1430.

Slepian D., 1983: Some comments on Fourier analysis, uncertainty and modeling, SIAM Rev., 25(3), 381--393.

Wahr J., F. Bryan and M. Molenaar, 1998: Time variability of the Earth's gravity field: Hydrological and oceanic effects and their possible detection using GRACE, J Geophys. Res., 103(B12), 30,205-30,229.

Wunsch C. and E.M. Gaposchkin, 1980: On using satellite altimetry to determine the general circulation of the oceans with application to geoid improvement, Rev. Geophys., 18, 725-745.

Wunsch C. and D. Stammer, 1998: Satellite altimetry, the marine geoid, and the oceanic general circulation, Ann. Rev. Earth planet. Sci., 26, 219-253.

Wang X., 2007: Global Filtering of Altimetric Sea Surface heights, Master Thesis on TU München, Institut für Astronomische und Physikalische Geodäsie.

Zenner L., 2006: Zeitliche Schwerefeldvariationen aus GRACE und Hydrologiemodellen, Diplomarbeit on TU München, Institut für Astronomische und Physikalische Geodäsie.

[1] http://www.gfz-potsdam.de/GRACE/results/grav/g004-eigen-cg03c.html

Acknowledgement